

Department of Physics and Astronomy  
University of Heidelberg

**Diploma Thesis in Physics  
2010**

submitted by  
Rebecca Boll  
born in Hagen



# A Monolithic Active Pixel Sensor as Direct Monitor for Therapeutic Antiproton and Ion Beams

This diploma thesis has been carried out by  
Rebecca Boll

at the  
Max-Planck-Institute for Nuclear Physics in Heidelberg

under the supervision of  
Prof. Joachim Ullrich

Heidelberg, December 1, 2010



## **A Monolithic Active Pixel Sensor as Direct Monitor for Therapeutic Antiproton and Ion Beams**

The *Mimotera*, a monolithic active pixel sensor (MAPS) of crystalline silicon has been investigated regarding its ability to directly monitor antiproton and ion beams, and has been implemented as a beam monitor at the Antiproton Cell Experiment (ACE) at the European Organization for Nuclear Research (CERN). It has been proven to be a well-suited device for monitoring a spill of about  $3 \times 10^7$  antiprotons only 500 ns long, on a shot-to-shot basis in real time without saturating. The commissioning of the *Mimotera* at ACE represents a major improvement, ensuring not only a more reliable data analysis due to exact profile measurements, but also speeding up the initial preparation of the experiment significantly.

Moreover, it has been shown that the *Mimotera* behaves linearly as a function of intensity, as well as of the energy loss of a carbon ion beam at the Heidelberg Ion-Beam Therapy Center (HIT). The readout rate of the system is high enough to track fluctuations in the beam intensity during one spill, such that the *Mimotera* could also serve as a tool for fast and reliable quality assurance in hadron therapy facilities.

## **Ein monolithischer, aktiver Pixelsensor als direkter Monitor für Antiprotonen- und Ionenstrahlen**

Der *Mimotera* Detektor, ein monolithischer, aktiver Pixelsensor aus kristallinem Silizium wurde hinsichtlich seiner Eignung als direkter Monitor für Antiprotonen- und Ionenstrahlen untersucht. Er wurde im Antiproton Cell Experiment (ACE) an der Europäischen Organisation für Kernforschung (CERN) als Strahlmonitor installiert und es wurde gezeigt, dass der *Mimotera* geeignet ist, einzelne Antiprotonenschüsse von nur 500 ns Länge und einer Intensität von etwa  $3 \times 10^7$  Teilchen abzubilden, ohne dabei in Sättigung zu gehen. Dies bietet eine erhebliche Verbesserung für ACE, da der Detektor nicht nur eine verlässlichere Datenanalyse durch genaue Profilmessungen ermöglicht, sondern außerdem auch das Einstellen des Strahls zu Beginn des Experimentes deutlich beschleunigt.

Weiterhin wurde gezeigt, dass der *Mimotera* sich linear als Funktion der Intensität und des Energieverlustes eines Kohlenstoffionenstrahls am Heidelberger Ionenstrahl-Therapiezentrum (HIT) verhält. Die Ausleserate des Systems ist hoch genug, um ein Verfolgen der Intensitätsfluktuationen in jedem einzelnen Spill zu ermöglichen. Daher ist der *Mimotera* ein vielversprechendes Instrument, um die Qualitätssicherung in Hadronentherapiezentren zu verbessern.



# Contents

<b>1</b>	<b>Motivation</b>	<b>1</b>
1.1	Development of Hadron Therapy for Cancer Treatment . . . . .	1
1.2	The Antiproton Cell Experiment . . . . .	6
1.3	Goal of this Thesis . . . . .	8
<b>2</b>	<b>Comparison of Beam Monitoring Systems</b>	<b>9</b>
2.1	Previously Used Systems at ACE . . . . .	9
2.2	Semiconductor Radiation Detectors . . . . .	11
2.2.1	Basic Functionality . . . . .	11
2.2.2	Different Types of Silicon Detectors . . . . .	15
<b>3</b>	<b>The Mimotera</b>	<b>19</b>
3.1	Architecture of the Sensor . . . . .	19
3.2	Data Acquisition . . . . .	21
3.3	Data Analysis . . . . .	24
3.4	Why the Mimotera is the System of Choice . . . . .	27
<b>4</b>	<b>Antiproton Beam at ACE</b>	<b>31</b>
4.1	The Challenge of Saturation . . . . .	31
4.2	Beam Monitoring . . . . .	38
4.3	The Mimotera as an Alignment Tool . . . . .	41
<b>5</b>	<b>Ion Beams at HIT</b>	<b>43</b>
5.1	Experimental Conditions at HIT . . . . .	43
5.2	Carbon Ions . . . . .	45
5.3	Protons . . . . .	50
<b>6</b>	<b>Open Questions and Summary</b>	<b>53</b>
6.1	Radiation Damage . . . . .	53
6.2	Summary and Outlook . . . . .	57
<b>A</b>	<b>Mimotera Manual for ACE</b>	<b>61</b>
A.1	Setting up the system . . . . .	61
A.2	Taking Data . . . . .	63
<b>B</b>	<b>Bibliography</b>	<b>69</b>



# 1 Motivation

## 1.1 Development of Hadron Therapy for Cancer Treatment

The most common type of radiation currently used for tumor therapy are photons in form of X-rays. Photons lose their energy when traversing matter via three different mechanisms: Photoelectric effect, Compton scattering or pair production. The probability of the occurrence of each of these processes depends on the energy of the photon, as can be seen in Fig. 1.1. X-rays with energies below 120 keV are most likely to undergo Photoelectric effect. All of the interactions are destructive, such that the beam intensity is reduced exponentially with increasing depth in the target.

However, most tumors are deep-seated in the body. Delivering photons deeper into the patient is only possible by increasing their energy significantly. This leads to a so called build-up effect in the dose, shifting the location of maximum energy deposition from the surface deeper into the target by some centimeters, as illustrated in Fig 1.2. The reason for this is the fact that a photon delivers all of its energy to one particle (or two, in case of pair production), resulting in relatively high-energetic electrons. Those have a certain probability to leave the target volume through the front surface, and, therefore do not contribute to the deposited dose. This process is possible from within deeper depths in the target, when the photon energy increases, the energy delivered to the tumor is increased, and unwanted effects in the entrance channel are reduced. Nevertheless, entrance doses still have to be relatively high to cause an effect to the actual cancer, damaging significantly the surrounding healthy tissue, and often lead to limitations of the achievable dose.

Modern X-ray technologies like Intensity Modulated Radiation Therapy (IMRT) attempt to mitigate these problems by overlapping several individual beams under different angles in the target volume. But even then the total energy to normal tissue remains higher than the energy deposited in the target.

In the last 60 years a new technology has been developed that is especially beneficial for the treatment of deep-seated tumors and which is in clinical use since 1990 [3]: The treatment of cancer with hadron beams, most commonly with protons, or, more recently, with carbon ions. Ions have one outstanding advantage over photons when considering their clinical application, namely the mechanism of energy loss along their path through the body. When a heavy charged particle hits a target, it loses

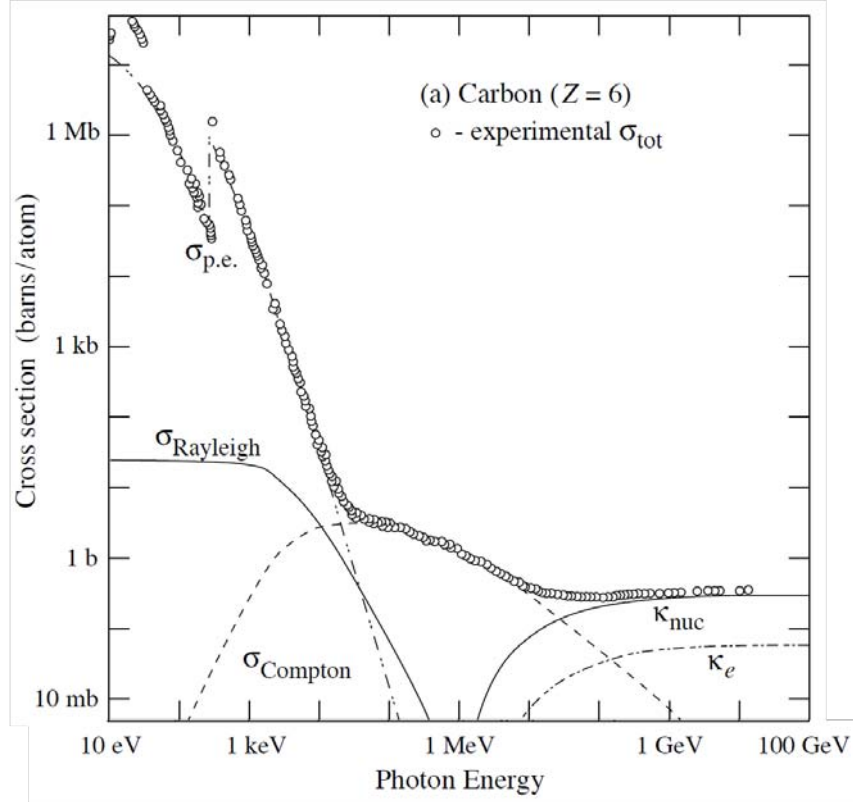


Figure 1.1: Total cross section of photon interactions in carbon and its composition from the different processes.  $\sigma_{\text{p.e.}}$ : Photoelectric effect,  $\sigma_{\text{Rayleigh}}$ : Rayleigh-scattering,  $\sigma_{\text{Compton}}$ : Compton-scattering,  $\kappa_{\text{nuc}}$ : Pair production, nuclear field,  $\kappa_e$ : Pair production, electron field. [1]

most of its energy via Coulomb-interactions with the electrons, resulting in excitation or ionization of the target atoms. Most importantly, it is not annihilated and continues to penetrate and to deposit energy. The Bethe-equation (1.1) describes the averaged energy loss per path length for heavy charged particles due to collisions with electrons in the region between  $0.1 \leq \beta\gamma \leq 1000$ , [1] with  $\beta\gamma = p/Mc$ ,  $\beta = v/c$ , with  $c$  the velocity of light and  $v$  the speed of incident particle,  $\gamma$  is the relative factor  $\gamma = 1/\sqrt{1 - \beta^2}$ ,  $p$  is the momentum of the incident particle, and  $M$  is the mass of the particle. [4]

$$-\frac{dE}{dx} = \frac{4\pi n(ze)^2(Ze)^2}{m_e v^2} \left[ \ln \frac{2m_e v^2}{I[1 - \beta^2]} - \beta^2 \right] \quad (1.1)$$

Here  $n$  is the electron density in  $\text{cm}^{-3}$ ,  $ze$  the charge of incident particle,  $Z$  the atomic number of absorber,  $m_e$  the electron mass, and  $I$  the mean excitation potential of the target atoms.

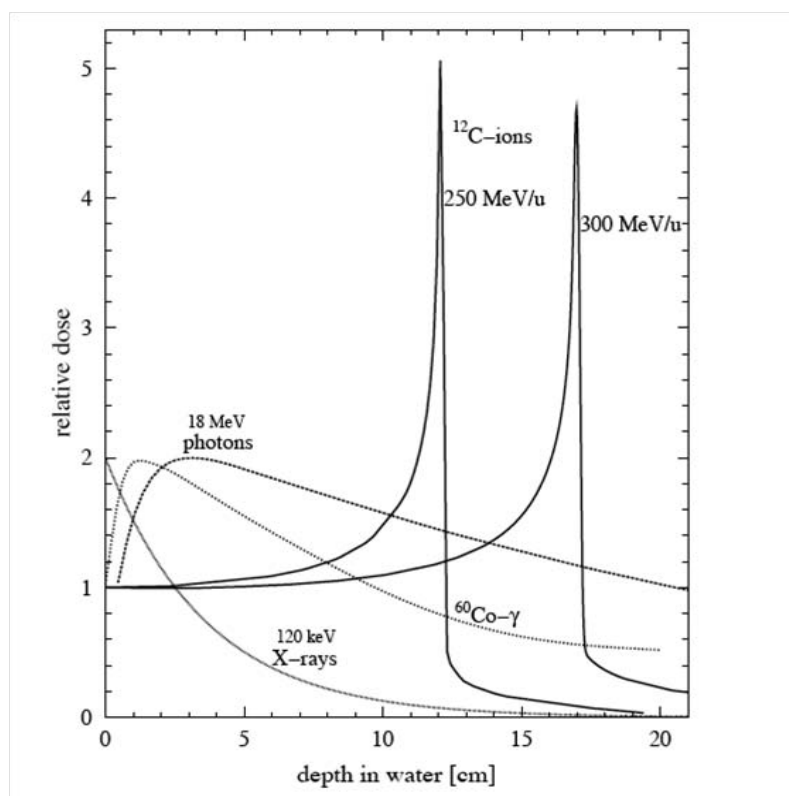


Figure 1.2: Depth dose curves of photons and carbon ions of different energies in water. [2]

The Bethe-equation results in the characteristic specific energy loss behavior of ions, as is illustrated in Fig. 1.3. It does not depend on the mass of the projectile, but only on its charge and speed, and on the density of the target material. At  $\beta\gamma \approx 3$  a minimum is observed, and projectiles of that energy are often called “minimum ionizing particles”. It occurs since  $dE/dx$  is proportional to  $1/v^2$  for lower energies, while for relativistic energies the logarithmic part of the equation becomes dominant. Particle energies for clinical applications lie below the minimum. This is advantageous for tumor therapy, because the energy deposition rises sharply for decreasing energies, which means that ions lose the largest fraction of their energy at the very end of their track, just before they are completely stopped in the target. This steep rise and the corresponding sharp maximum in the dose distribution, see Fig. 1.2, is called the Bragg-peak and was first discovered in 1904 by W.H. Bragg, while studying the absorption of  $\alpha$ -particles [5]. Due to this characteristic behavior it is possible to deliver energy to a deep seated tumor in the body, without unduly affecting the healthy tissue in front of it.

According to the type of heavy charged particle that one uses, the shape of the Bragg-peak and its relative height change somewhat, as can be seen in Fig. 1.4.

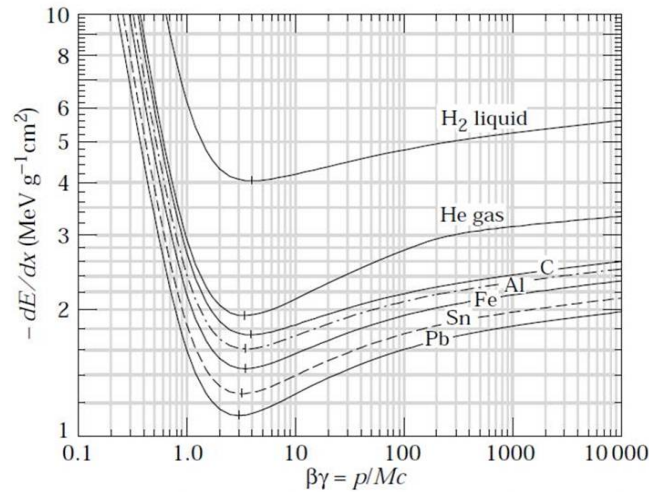


Figure 1.3: Specific energy loss of ions in different materials. [1]

Relative to the energy loss in the entrance channel, protons have a lower maximum energy deposition as compared to carbon ions, but the cut-off after the peak is sharp. Carbon ions deliver a higher maximum energy at the cost of a tail behind the peak caused by nuclear fragmentation of the projectiles. Both particle types are currently used for cancer treatment.

The idea of using antiprotons for cancer therapy, however, is rather new [7] and there is only one experiment worldwide performing research on this topic: The Antiproton Cell Experiment (ACE) [8], located at the Antiproton-Decelerator (AD) [9] of the European Organization for Nuclear Research (CERN). For details see section 1.2.

The physical behavior of antiprotons is nearly identical to protons, but with one crucial difference: Once the antiproton annihilates with a target proton at the end of its range, it releases additional energy of  $2 \times 936 \text{ MeV} = 1.87 \text{ GeV}$  per particle as compared to protons, of which a small but clinically significant fraction is deposited locally. This advantage can be seen in Fig. 1.4: The maximum energy delivered in the Bragg-peak is nearly twice as high for antiprotons, as compared to protons. This means that in order to achieve the same energy transfer to the tumor in the Bragg-peak region, only half as many particles are needed. The dose in the entrance channel in front of the tumor is reduced, accordingly sparing healthy tissue and organs at risk. However, this comes at the expense of a smeared out cut-off after the Bragg-peak and at the lateral edges of the target volume, caused by the secondary particles released during the annihilation. This has to be further investigated in order to make sure that no undesired effects occur that would cancel, or even dominate the potential clinical advantages of the increased energy deposition in the target.

A second advantage of antiprotons is the opportunity to track the irradiation in real-time: Apart from other particles, the annihilation of proton and antiproton

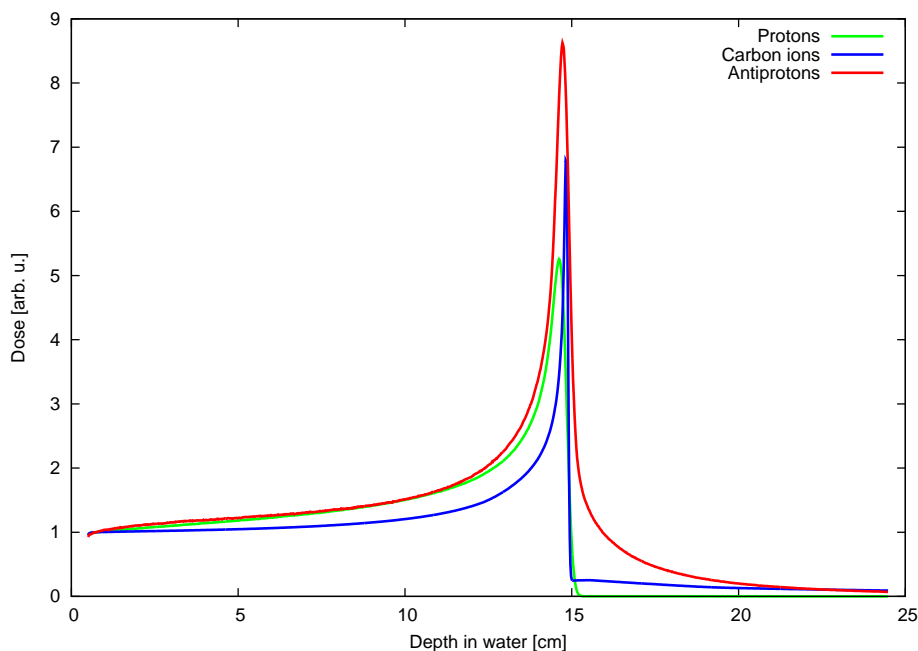


Figure 1.4: Bragg peaks in water for protons, antiprotons and carbon ions, normalized to the entrance channel. [6]

creates mostly pions. Those can be used for tracking the annihilation vertex and could therefore serve for quality assurance of the irradiation. A proof of principle for this method has been shown recently in the framework of the diploma thesis by Stefan Sellner. [6]

Monitoring of the beam is also possible for carbon ion irradiations, due to nuclear fragmentation of the projectiles leading to radioactive nuclides in the tissue. The creation of  $^{11}\text{C}$ , a  $\beta^+$ -emitter, is exploited in positron emission tomography (PET). Nevertheless, due to the half-life of  $^{11}\text{C}$  of 20 min, the time required to accumulate sufficient activity is too long to provide a real-time image during the treatment. The effect can therefore only be used for inter-fractional imaging. If a deviation of the distribution from the predicted treatment plan is observed, a correction can be applied to the next fraction of the irradiation.

As a potential drawback for antiproton therapy, the availability of the particles is obviously not at all trivial, and just two institutions worldwide, the Fermi National Accelerator Laboratory (Fermilab) and CERN produce a significant large number of antiprotons. Only CERN provides an energy interesting for biological applications. This is why irradiation of tumors with antiprotons will presumably never be a replacement for the existing methods, but it can be beneficial and of decisive importance for very complex situations, like tumors next to sensitive organs, or where previous irradiations already have caused a radiation load to the surrounding tissue close to the tolerance level.

## 1.2 The Antiproton Cell Experiment

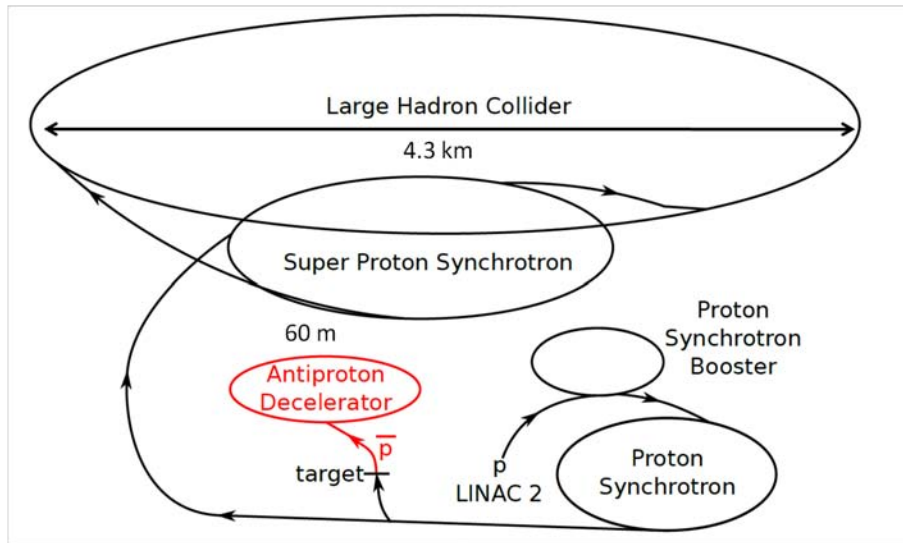


Figure 1.5: CERN accelerator complex.

The Antiproton Cell Experiment is dedicated to investigations of an innovative approach for cancer therapy. It is located at the Antiproton Decelerator (AD) at CERN, see Fig. 1.5. The antiprotons are produced by shooting 26 GeV/c protons coming from the Proton Synchrotron on an Iridium target. The maximum yield of antiprotons produced in this collision lies around 3.6 GeV/c, and antiprotons in a narrow band around this momentum are captured by a magnetic horn and injected into the Antiproton Decelerator. They are decelerated and cooled in several steps. Once a kinetic energy of 126 MeV (502 MeV/c momentum) is reached, they are ejected to ACE. Usually the antiprotons are decelerated to 5 MeV (100 MeV/c) and are sent to the three main experiments operating at the AD, studying antihydrogen.

The experimental set-up is displayed in Fig. 1.6: The antiproton beam enters a PMMA tank; in its center, along the central beam axis, PMMA tubes filled with V79-WNRE Chinese Hamster cells embedded into gelatin are placed. The usage of these special cells allows correlations to experiments with other radiation modalities, because they are used worldwide in a variety of different clinical tests. [10] The beam energy can be decreased to obtain a spread-out Bragg peak, by inserting a certain number of PMMA-degraders in front of the tank. The other devices displayed in Fig. 1.6 are used for beam monitoring and are explained in detail in section 2.1.

The volume in the tank around the tube is filled with a mixture of water and glycerin, providing cooling to 4° C for the cells, to halt any repair mechanism and thereby to compensate for sometimes very long irradiation times due to the low dose rate of  $\approx 20$  mGy/min. Moreover, the fluid simulates the back scattering from the tissue surrounding the actual irradiated cells, which also takes place in a real biological

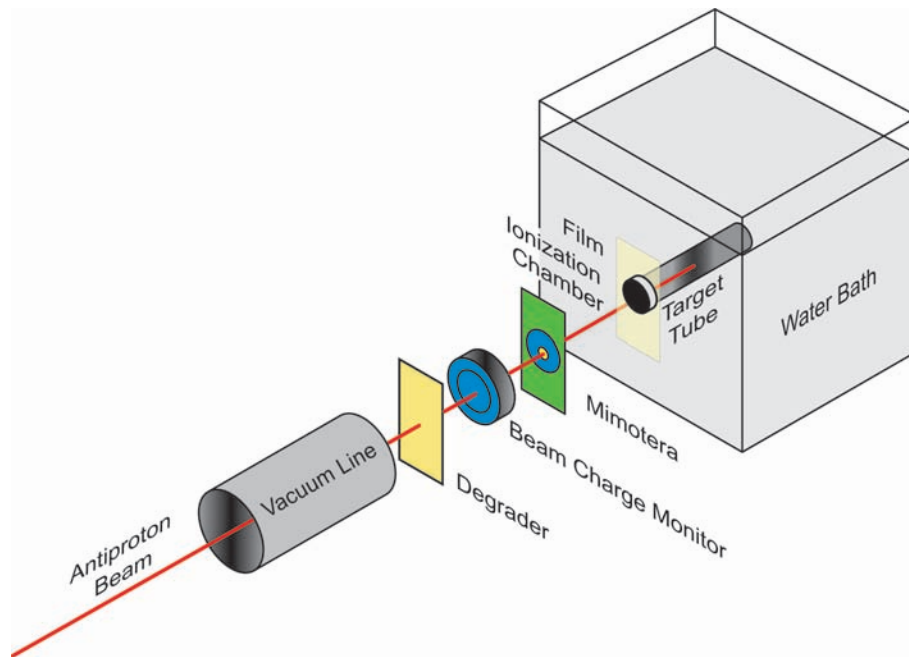


Figure 1.6: ACE experimental set-up.

target. Some of the annihilation products, for example alpha-particles or neutrons have a certain probability to be scattered back into the target volume and deposit additional dose in the sample. Without the surrounding bath, this contribution to the total dose would be lost at ACE. The density of the fluid is chosen to be identical to the density of the cell sample, to avoid any artifacts. The beam diameter is larger than the actual sample size, and antiprotons traveling parallel outside the cell tube in a medium with different density, would have Bragg-peaks at a different range. The secondary particles from the annihilation would then modify the dose distribution in the sample.

After the irradiation, cell survival curves are obtained from evaluating the probes. As the biological effect of particles on living cells is the quantity to be evaluated, it is crucial to know as precisely as possible the physical characteristics of the incident beam. They serve as input parameters for calculating the exact dose received by the individual slices of the cell sample along the beam axis, using a Monte Carlo program based on a FLUKA simulation (FLUKA = “FLUktuierende KAskaden”).

The situation at ACE is unique in the sense of the spill structure: The beam of antiprotons is pulsed, one spill is 500 ns long and arrives only every 90 s due to the accelerator operation. During these 500 ns, the flux is about  $3 \times 10^7$  particles, which leads to a momentarily integrated intensity of  $3 \times 10^7 / 500 \text{ ns} = 6 \times 10^{13} / \text{s}$ . The beam energy is 126 MeV, and was chosen to provide a penetration of approximately 11 cm water equivalent depth.

## 1.3 Goal of this Thesis

For the rather special situation at ACE, a detector is required, that is able to obtain the exact characteristics of the antiproton beam. Two tasks shall be accomplished by the new system: First of all it shall track the beam during all cell irradiation experiments, in order to provide a reliable input for the dose delivered to the sample in the analysis of the cell survival curves. The main properties that have to be known for an evaluation of the data are:

- The **beam profile**: Non-Gaussian, asymmetric beam profiles can lead to inhomogeneous dose distributions, which need to be considered for the cell survival.
- The **beam intensity**: The number of particles delivered to the cell sample has to be known. Beam spills with particle numbers reduced down to 60% of the nominal intensity have been observed, see chapter 4, that need to be included in the analysis. Therefore a shot-to-shot tracking of the intensity fluctuations is needed.
- The **beam position**: Shifts of several millimeters have been observed which would lead to an incorrect estimation of the delivered dose, if disregarded.

A challenge for the detection system will be to measure the correct number of particles for each pixel and not to saturate due to the high flux impinging within a very short time interval. Furthermore it must provide a fast, digital output for every single shot. Previous set-ups did not satisfy these requirements, as explained in section 2.1.

Secondly, the detector shall not only be applied for tracking the beam, but also to speed up the preparation of the experiment. For the one week of beam time which the ACE experiment is granted each year, the operation of the Antiproton-Decelerator has to be modified significantly because the beam energy is changed from the standard value of 5 MeV to 126 MeV for the cell irradiations. This makes the preparation of the experiment rather complicated and tedious. For the alignment of the beam with respect to the experiment, a device is needed that can provide a shot-to-shot, real-time image of the beam, and can be accessed in the accelerator control room, to allow the AD operator team to modify the current settings of the steering and focusing magnets in the ACE beam line.

The lack of a detector that has all the required characteristics gave rise to the search for a new device. This thesis is dedicated to the installation and commissioning of the *Mimoto*, a Minimum Ionizing *MO*nolithic active pixel detector for the *TERA* foundation [11] in the Antiproton Cell Experiment, to be applied as a beam monitor for the run in October 2010 and all future beam times. Furthermore, the more general applicability of the *Mimoto* in clinical facilities for hadron therapy with protons and carbon ions is investigated.

## 2 Comparison of Beam Monitoring Systems

### 2.1 Previously Used Systems at ACE

Previous set-ups at ACE included different systems for monitoring intensity and shape of the beam. Tab. 2.1 gives an overview, including the characteristics required for ACE.

	Beam charge monitor	Ionization chamber	Gafchromic film	Scintillator + camera	Mimotera
Spatial resolution	–	–	x	x	x
Linear digital output	x	x	–	–	x
Sensitive to single spill	x	x	–	–	x
Real-time image	–	–	–	–	x

Table 2.1: Beam monitoring systems at ACE.

#### Beam Charge Monitor<sup>1</sup>

This device consists of an Integrating Current Transformer that is placed in front of the water tank, as can be seen in Fig. 1.2, and the actual Beam Charge Monitor (BCM). The BCM processes the signal obtained from the transformer, producing a bipolar voltage that is directly proportional to the beam charge, and holding it for  $500 \mu\text{s}$ . This output provides a reference for the number of particles in each beam spill. The resolution of the system is  $1 \text{ pC}$ , corresponding to  $3 \times 10^6$  antiprotons. [12] For the intensity at the ACE beam line of  $3 \times 10^7$  particles per pulse, the signal to noise ration is thus only about 10, the system does not provide sufficient precision. Also it has no position resolution and can therefore not serve as a monitor for the beam profile.

<sup>1</sup>BCN-IHR; Bergoz Instrumentation, St. Genis, France.

### **Ionization Chamber<sup>2</sup>**

An ionization chamber, read out by an electrometer, is placed directly in front of the water tank. The current is linearly proportional to the number of particles in the beam, and moreover, the chamber is calibrated to an absolute dose measurement. Therefore, it provides more information than the beam charge monitor and is also more precise. Nevertheless, it does not have any position resolution, as the signal is integrated over the entire volume.

### **Gafchromic Film<sup>3</sup>**

This is a special kind of film that darkens when irradiated by ionizing radiation. [13] It is taped on the entrance window of the water tank and provides the position of the beam. The darkness of the film is proportional to the delivered dose, which is linearly related to the number of particles. Unfortunately, about twenty shots are needed until the picture is dark enough to be evaluated. For the ACE spill structure, this means that one has to wait for half an hour to see if the beam position was well adjusted, which is not a real-time image and cannot detect shot-to-shot fluctuations of intensity or position. Moreover, the signal is not available as a digital output, but the film has to be scanned and analyzed off-line.

### **Scintillator<sup>4</sup>**

This is the set-up which was used at ACE up to 2006, consisting of a scintillating screen placed in front of the entrance window of the water tank. This screen was viewed by an intensified CCD camera, placed under a 45 degree angle outside the beam path. It had the required position resolution, and was able to provide single shot images for the initial experiments at 50 MeV beam energy. Nevertheless, as the light yield was already poor for this low energy, for the current measurements at 126 MeV it is much too low to provide an image for a single shot of antiprotons. Choosing a thicker scintillator would presumably not improve this considerably, because the generated photons have to leave the surface to be detected by the CCD camera, which is suppressed for a thick volume.

---

<sup>2</sup>ROOS type, read out by a UNIDOS; both PTW, Freiburg, Germany.

<sup>3</sup>Gafchromic<sup>TM</sup> EBT-2 film; International Specialty Products, Wayne, New Jersey, USA.

<sup>4</sup>BC 400 Scintillator Sheet; Saint-Gobain Ceramics & Plastics Inc., Paris, France.

None of the systems used up to now meets all the requirements for a real-time beam monitor. A recently founded cooperation with Prof. Massimo Caccia from the Università dell' Insubria in Como, Italy, gave rise to the idea of using the newly developed *Mimotera*, a thin semiconductor pixel detector of crystalline silicon, placed directly in the beam. It is supposed to fulfill all the requirements at ACE, as claimed beforehand in Tab. 2.1. Section 2.2 gives a short introduction in the basics of semiconductor radiation detection in general, and chapter 3 explains in detail the architecture and the operation principle of the *Mimotera*.

## 2.2 Semiconductor Radiation Detectors

### 2.2.1 Basic Functionality

In the following, all working principles will be explained for silicon, as it is the most commonly used semiconductor for the fabrication of radiation detectors. Nevertheless, other materials like gallium arsenide have similar properties.

#### Properties of Silicon

Silicon detectors are used for the detection of charged particles or photons in many different applications. The basic principle is always the same, although the design of a specific detector can vary significantly. Silicon is a semiconductor with diamond crystal structure, a lattice constant of  $5.43 \text{ \AA}$ , and a band gap of  $E_g = 1.12 \text{ eV}$ , see Fig. 2.1. [15] As silicon is an indirect semiconductor, the production of an electron-hole pair requires a larger energy, on average  $3.62 \text{ eV}$  at room temperature [16] because additional phonon scattering is needed for the direct transition, as also illustrated in Fig. 2.1. Therefore, the incidence of this process is suppressed. Silicon is sensitive to a wide range of ionizing radiation, including visible light ( $E \approx 2\text{--}4 \text{ eV}$ ) and X-rays, as well as ions or high-energy electrons.

At absolute zero, a semiconductor is an insulator, but at finite temperatures the conduction band is occupied by thermally excited electrons, leaving behind holes in the valence band. The amount of electrons in the conduction band is given by the Fermi-Dirac statistics. At room temperature only a fraction of 1 out of  $10^{12}$  atoms is ionized. [17]

#### p-n-Junction

In principle, pure silicon could serve as a detector for ionizing radiation: Electrons from the valence band are excited to the conduction band and can be measured as a current. However, for technical applications the current is too low because the intrinsic charge carrier density is much too small. It can be increased by doping as

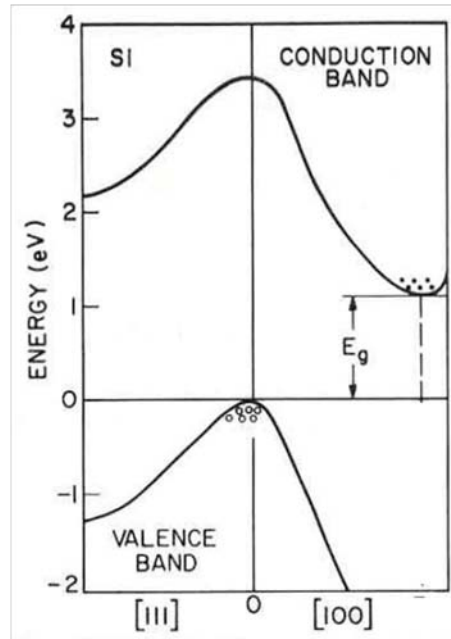


Figure 2.1: Band structure of silicon. [14]

illustrated in Fig. 2.2. Either elements of group III of the periodic table with energy bands close to the valence band are added as acceptors (p-type), or elements of group IV, having levels close to the conduction band are added as donors (n-type). The energy gap between the band and the Fermi-energy is then small enough, such that even at room temperature one electron (hole) per dopant atom is created in the conduction (valence) band, resulting in a significant charge carrier density that behaves like a free electron (hole) gas. Heavily doped material is denoted as  $n^+$  or  $p^+$ . Layers of this kind of material have very high conductivity, and can therefore be used as an electrical contact.

If p-type and n-type regions are connected, a p-n-junction is created, as shown in Fig. 2.2. Where they get in contact, the different charge carriers recombine and the different Fermi-energies of the two sections converge. A depletion region without free charge carriers is created, containing a positive space charge in the n-type part and a negative space charge in the p-type part. The diffusion stops, as soon as the electric field  $\mathcal{E}$  compensates the difference in charge carrier densities. The resulting potential across the depletion region is called built-in-voltage [16]. If the concentration of donors in the n-type material is higher than the concentration of acceptors in the p-type part, the depletion region extends farther into the p-type side of the junction. Because there are no free charge carriers, but only stationary ions left in the depletion region, it has a very high resistivity.

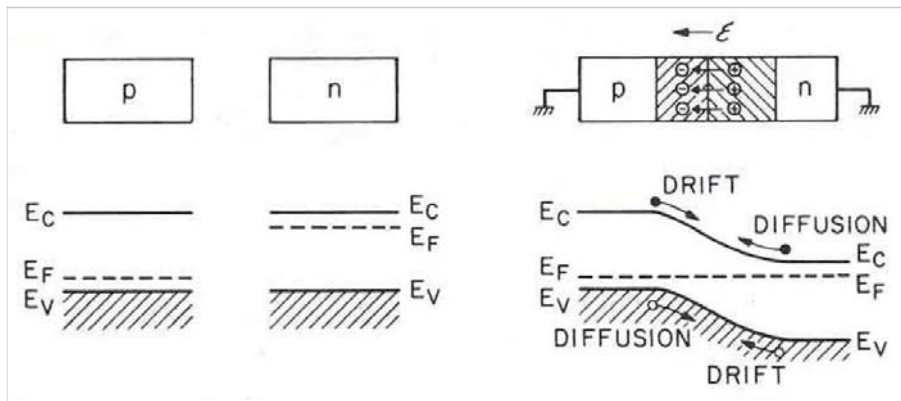


Figure 2.2: p-n-junction ( $E_C$ : Energy level of conduction band,  $E_V$ : Energy level of valence band,  $E_F$ : Fermi-energy). [14]

In practice a junction cannot be achieved by simply pressing the two types of material together, but is created by implanting donors or acceptors from one side into a single crystal. If a charged particle hits the depletion region, it creates electron-hole pairs like in pure silicon, but due to the electric field the charge carriers are separated, electrons and holes drift in different directions.

### Position Resolution

For most physical applications, position resolution is needed. This can be achieved by different kinds of segmentation: Single or double sided strip detectors, see Fig. 2.3, can be used as long as the particle flux is not too high. Otherwise ambiguities occur when the readout time is longer than the time between two hits. As soon as two x- and two y-coordinates are measured at the same time, it is no longer clear which two of them belong together.

Under these circumstances, pixel detectors, see Fig. 2.4, are more useful. They provide a two-dimensional resolution, because either the p<sup>+</sup>-part or the n<sup>+</sup>-bulk contact is divided into pads. Each pixel is connected to a single electronic readout. For particle counting it is usually operated in a binary mode, in the sense that it gives out a normalized signal if a particle was traversing and gives out no signal otherwise. However, it is also possible to achieve an energy resolution by evaluating the pulse height, as frequently done in solid state photon detectors. The detector can be used for particle tracking (counting individual particles), imaging (integrating multiple particles), as well as for spectroscopy, if less than one particle or photon hits a pixel per readout cycle. See also analog and counting mode in 3.3.

## Advantages and Disadvantages

Silicon detectors have a very good energy resolution because of the small ionization energy of 3.6 eV, compared to 15 – 30 eV for gas ionization chambers. Also, their dimensions can be much smaller, as they have a higher stopping power as compared to a gas-filled detector, such that excellent position resolution and high sensitivity e.g. to minimum ionizing particles can be achieved. The readout can be very fast, for example 10 kHz frame rate for the Mimotera, and an immediate and direct electronic record of each event is provided. The sensors have rather little dead material, the entrance window is very thin, especially for the Mimotera, see 3.1. Scintillators can also be built thin, but they have a worse energy resolution, typically  $\approx 10$  photons per keV of energy deposition for plastic scintillators. [18] Disadvantages of silicon detectors can be the rather high sensitivity to radiation damage, and their higher costs compared to gas chambers, especially when large areas are needed.

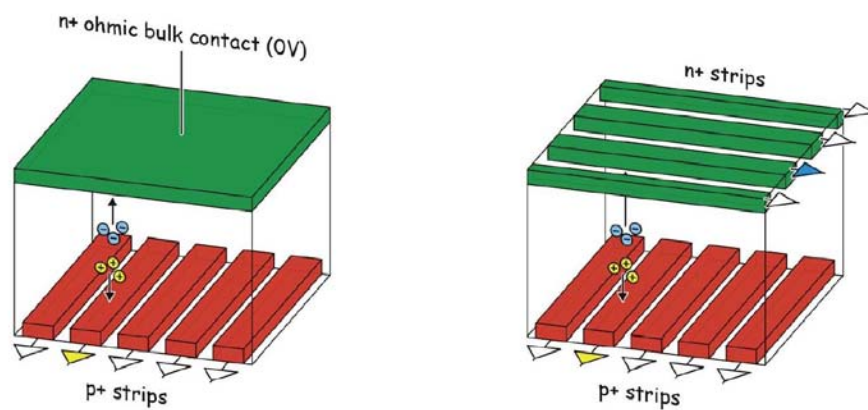


Figure 2.3: Single and double sided strip detector. [16]

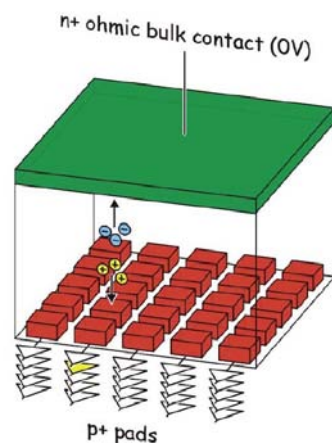


Figure 2.4: Pixel detector. [16]

## 2.2.2 Different Types of Silicon Detectors

### Charge Coupled Devices (CCD)

An example of a pn-CCD is shown in Fig. 2.5. It is used for detection of ionizing particles, for example in digital cameras. Charges are created in the fully depleted bulk. The neighboring strips lie on different potentials, such that the electrons are trapped in potential wells, they are shifted to the anodes in a serial readout. Because the lines are read out one after another, the required time is rather long and a problem of saturation arises if the incoming flux is so high that a potential well cannot gather all created electrons before the pixel has been read out.

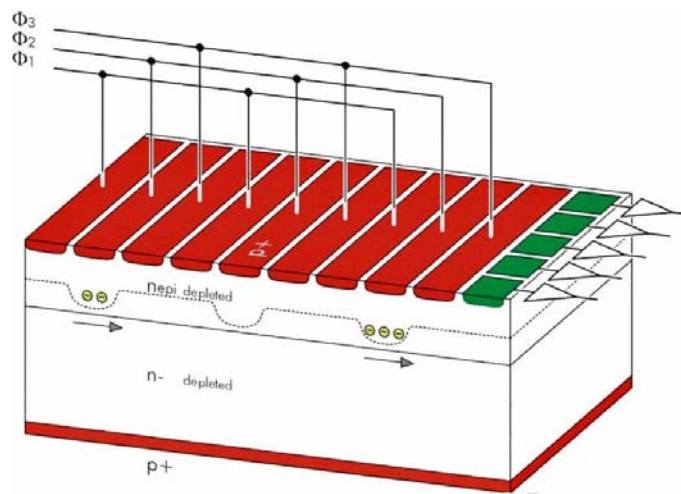


Figure 2.5: Charge Coupled Device. Readout anodes are green. [16]

### Hybrid Pixel Detectors

This type of detector consists of three parts, as illustrated in Fig. 2.6: The p<sup>+</sup>-n-junction as the sensor itself, a readout chip, and bump bonds, which build a connection between the sensor and the chip. Each pixel needs its own electronic readout channel. These types of silicon detectors are commonly used today, for example for inner-tracking systems in current high-energy experiments. They can be produced very thin, which is important in order not to have too much matter disturbing the tracks of the secondary particles from the collision events. These need to traverse to the outer layers of the detector systems, for example calorimeters, nearly unaffected in order to be able to reconstruct their path and to identify them correctly. The readout is fast and the detectors have a reasonable good radiation hardness. Nevertheless, the bonding process is rather complex and the price is high because of the three different components required.

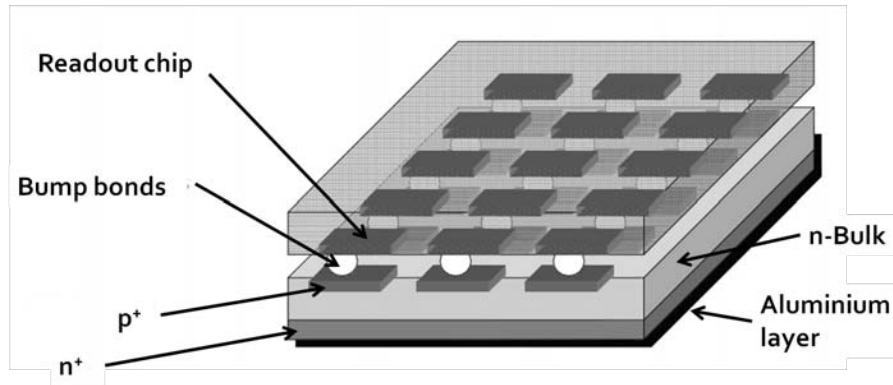


Figure 2.6: Hybrid pixel detector. [16]

### Monolithic Active Pixel Sensors (MAPS)

In contrast to the hybrid design, the monolithic pixel detector consists of only one part. The readout chip is integrated directly on the active layer of the sensor. Thus, interconnection between different components is not needed anymore. The detector is divided into three different parts, see Fig. 2.7. The substrate and the wells are very highly doped, whereas the p-type epitaxial layer is only mildly doped, undepleted and of low-resistivity. The name epitaxial layer hereby refers to the production technique of growing epitaxial layers of monocrystalline silicon.

If a charged particle passes, charge carriers are created in the epitaxial layer. They diffuse thermally, until they reach an area with an n-well which collects the electrons and gives out the signal. There is no external electric field applied at the active volume. The high doping of the  $p^+$ -wells causes potential barriers at the boundaries that force the free charge carriers to stay inside the epitaxial layer. This situation corresponds to the region marked by the red line in Fig. 2.7. The wells act as mirrors and reflect the electrons back inside the epitaxial layer, until they reach the n-well and are read out. This corresponds to the green line in Fig. 2.7.

These detectors can be build very thin, down to  $14\ \mu\text{m}$ , [19] the readout pitches are integrated and very small ( $5 - 50\ \mu\text{m}$ ). Disadvantages can be the rather small signal and the lower radiation hardness, as compared to hybrid pixel detectors. On the other hand, the small signal turns out to be an advantage for the purpose of using the sensor as a direct beam monitor for ACE, as pointed out in chapter 1 because the problem of saturation has to be overcome.

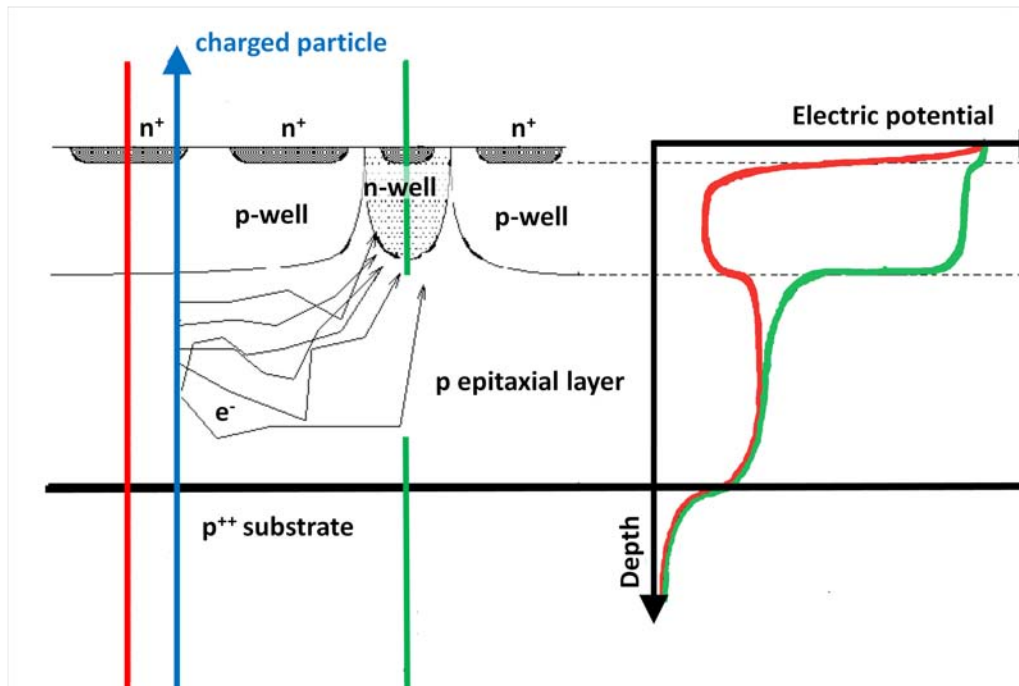


Figure 2.7: Principle of a monolithic active pixel sensor (modified from [19]).

This is the architecture of one readout diode. The green and red lines in the potential correspond to the green and red cross-sections in the sensor.

### Crystalline versus Amorphous Silicon

Apart from the architecture of a specific detector, one can use either crystalline or amorphous silicon as material for the sensor. A crystal has better properties regarding particle detection, as the structure is exactly known. Doping is much less efficient in amorphous material than in crystalline silicon: Defects, especially dangling bonds give rise to additional energy states in the band gap, which are often electrically active. The high concentration of these intrinsic defects prevents the Fermi-energy from shifting when doping the amorphous silicon. In addition to this, donors or acceptors with five or three valence electrons respectively, can keep their natural configuration in amorphous material, because there is no fixed structure which forces them to change their valence to four. Furthermore, the band gap is spread out because of the variation of bonding lengths in amorphous material.

One advantage of using amorphous silicon would be the better radiation resistance: In crystalline material radiation can cause defects like vacancies or interstitials, whereas in amorphous material there are no such effects because of the missing long-range order. Moreover, it is less expensive in production.



# 3 The Mimotera

## 3.1 Architecture of the Sensor

The *Mimotera* is a monolithic active pixel sensor of crystalline silicon. Its architecture can be seen in Fig. 3.1 and is patented under U.S. patent no. 7,582,875. The epitaxial layer is  $14\ \mu\text{m}$  thick and has an entrance window of only about  $100\ \text{nm}$ . [19] This is possible by attaching the original wafer to a supportive background of a few hundred micrometer of amorphous silicon, in a way that the electronic readout is buried. Then the wafer is thinned down from the backside, until only a very thin surface passivation layer covers the sensitive volume. The wire bonding to connect the electronics has then to be performed through etching holes in the surface. The sensor itself is mounted either on a printed circuit board (PCB) of about  $1.5\ \text{mm}$  thickness, or, if it should be operated in vacuum, on a ceramic support. This results in a total thickness of about  $2\ \text{mm}$  for the PCB system and less than  $1.5\ \text{mm}$  for the ceramic version. The electronic circuits on the two designs of the board differ, resulting in a slightly different behavior of the systems as will be seen in section 4.1. The chip is controlled by an external data acquisition board, which can be operated via LabView.

The sensor consists of  $112 \times 112 = 12544$  pixels, each of the size of  $153 \times 153\ \mu\text{m}^2$ , leading to an active area of  $17 \times 17\ \text{mm}^2$ . This area is divided into four sub-arrays of  $28 \times 112$  pixels that are illustrated in Fig. 3.2 and are read out in parallel with a frame rate up to  $10\ \text{kHz}$ .

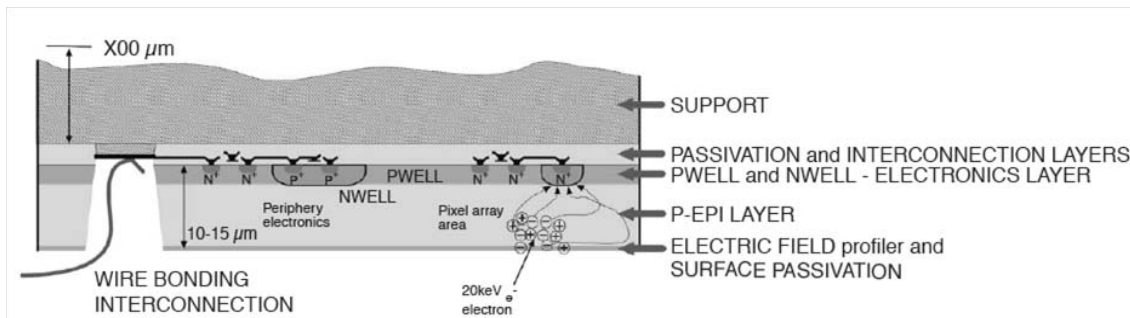


Figure 3.1: Cross-section of the Mimotera. [19]

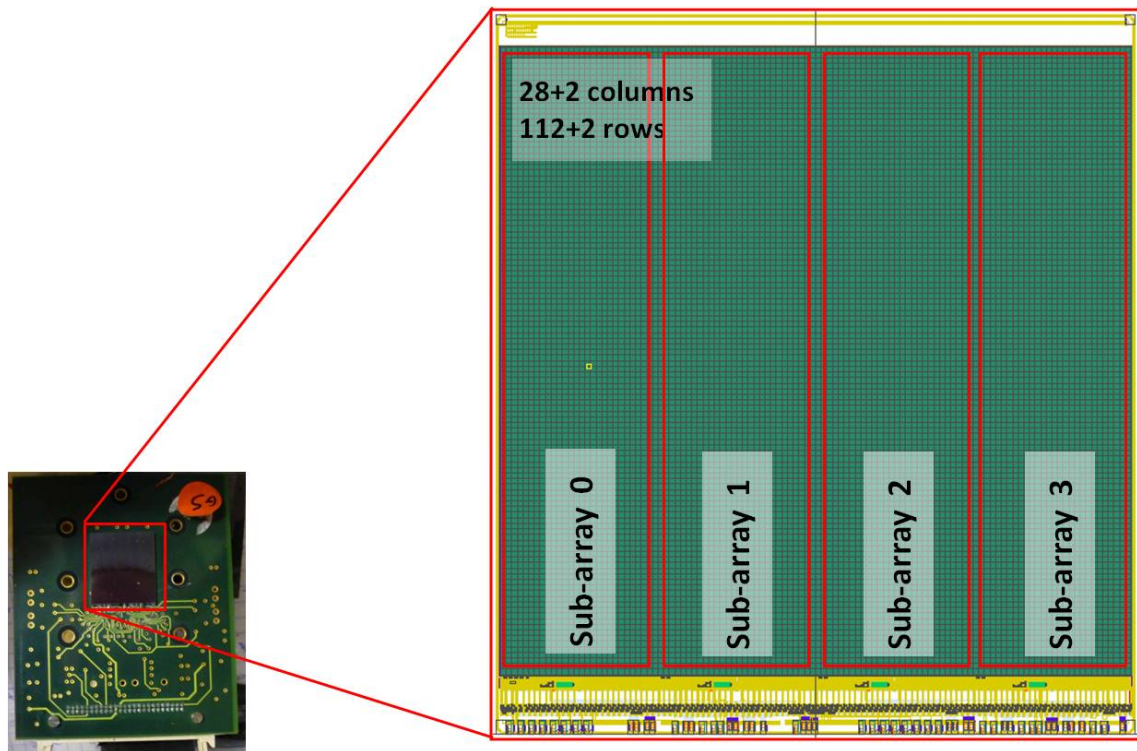


Figure 3.2: Photo and layout of Mimotera with PCB background. The two additional rows and columns are virtual marker pixels, as explained in section 3.2.

One feature makes the Mimotera a unique device: The design of one of its single pixels that consists of  $2 \times 81$  diodes,  $5 \times 5 \mu\text{m}^2$  each, as can be seen in Fig. 3.3. All of the red (filled squares) diodes are connected to each other, creating one readout matrix, the same holds for the yellow (squares with dots) diodes. These two interleaved matrices will be referred to as matrix A and matrix B in the following. This layout significantly reduces the diffusion of generated charge carriers from one pixel to the neighboring one, which is called crosstalk. In a classical design, one pixel is read out by one diode. Charges that are created at the edge of a pixel must travel a rather long way until they can be collected. This increases the risk of collecting electrons at a neighboring diode. The design of the Mimotera ensures reliable charge collection even at the edges of each pixel. Another advantage of this architecture becomes obvious when looking at the readout procedure of the system in section 3.2.

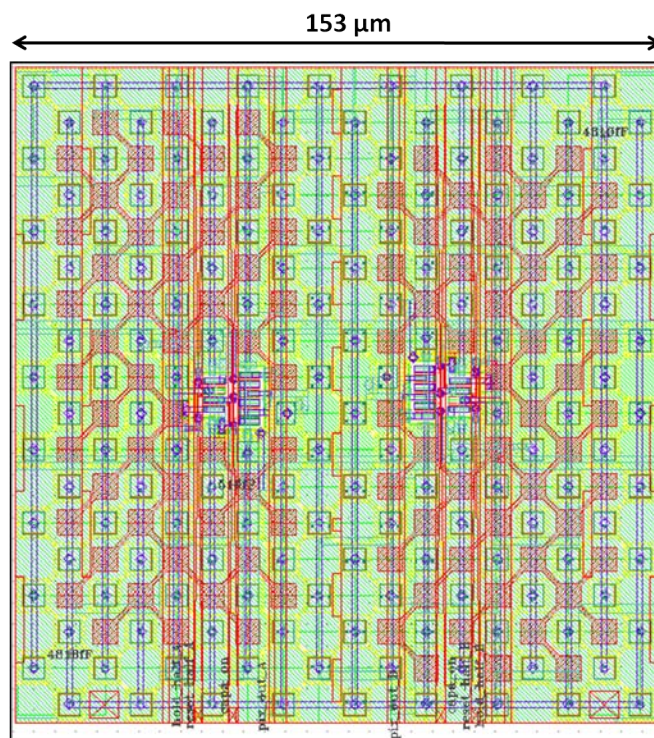


Figure 3.3: Layout of one single pixel of the Mimotera.

## 3.2 Data Acquisition

### Timing and Binary Data Structure

The division of the diodes of one pixel in two independent sub-matrices makes it possible to time their readout separately. The timing structure is shown in Fig 3.4. While matrix A is collecting the generated charge carriers, the charges stored in the diodes of matrix B are read out and the diodes are reset. In the next time interval, matrix B is collecting data and matrix A is read out. Hence, no charges get lost during the readout and it can be claimed that the Mimotera is free of any dead time. This feature is of crucial importance when trying to monitor clinical beams as discussed in chapter 5.

The maximum readout rate for one single pixel is 20 MHz, which corresponds to a minimum resolution of  $1/20 \text{ MHz} = 50 \text{ ns}$ . The serial readout of one sub-array therefore takes  $50 \text{ ns} \times (112 + 2) \times (28 + 2) = 171 \mu\text{s}$ , the additional two pixels in each dimension are marker pixels, see next paragraph. As the four sub-arrays operate in parallel, this is identical to the readout time for one frame for the whole detector. In most set-ups a clock rate of 2.5 MHz per pixel was chosen, which leads to an integration time for a full frame of 1.4 ms.

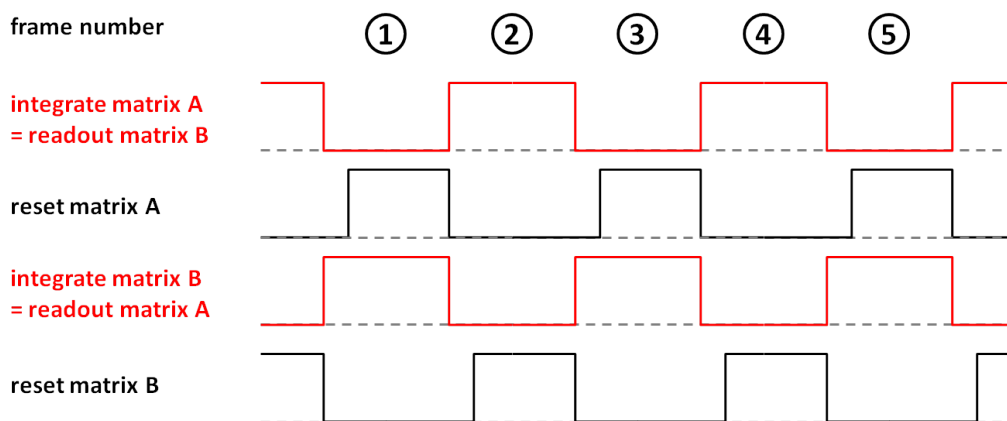


Figure 3.4: Relative timing of the two readout matrices of the Mimotera.

The signal of every pixel of the Mimotera is stored in a linear array, not two-dimensionally. The matching of the linear information with the two-dimensional spatial coordinate on the detector surface is carried out in the off-line analysis with the help of virtual marker pixels: At the beginning and at the end of each sub-matrix there is a row of 28 pixels with the maximum signal height of about  $-2000$  arb.u., and the quarters are separated by two columns with a signal of about  $+2000$  arb.u. These are not physical pixels, so there is no dead area on the sensor, but they are introduced electronically. The resulting linear signal and the corresponding matrix can be seen in Fig. 3.5, the marker pixels are clearly visible, as is one misbehaving pixel at about 9700. Note that the signal in the Mimotera is negative. Also visible is that the baseline in the fourth sub-quarter is different from the other three, this problem will be covered in section 4.

Fig. 3.6 explains the structure of the binary data file. One data file can have a size of up to 2 GB and is saved in a .dat format. It contains a series of events, each of which can consist of up to 38 frames, limited by the buffer on the data acquisition board. If running in triggered mode, one event is saved for each trigger pulse, see next paragraph. The frames themselves are an alternating sequence of single readouts of matrices A and B, the duration of one integration period is typically 1.4 ms. The information stored for each frame is the linear signal of the four sub-arrays shown in 3.5.

## Continuous versus Triggered Mode

The data can be saved to the file either in continuous, or in triggered mode. The operation of the sensor itself is not affected by this, it is continuously integrating and reading out the diodes with the clock rate chosen. Nevertheless, the data transfer to the PC is not possible with these high frequencies. Therefore, if running in continuous mode, events get lost randomly at any time the PC is still occupied

storing the previous event. In principle, the absolute time-stamp of each event can be reconstructed afterwards by evaluating the global frame number that is updated for every frame. For the needs at ACE, however, it is much more convenient to use the triggered mode, as only one specific frame is needed within 90 s. In the triggered mode the system still works continuously, but the saving of the data to a file is triggered. The buffer on the data acquisition board can store up to 38 frames, until the 1st frame is overwritten by the 39th. It is possible to save up to 32 frames before the trigger signal and 32 frames after the signal, but only a maximum of 38 frames for each event. For the measurements at CERN, 6 frames before and 32 after the trigger pulse were saved, such that the beam spill was always contained in frame number 7.

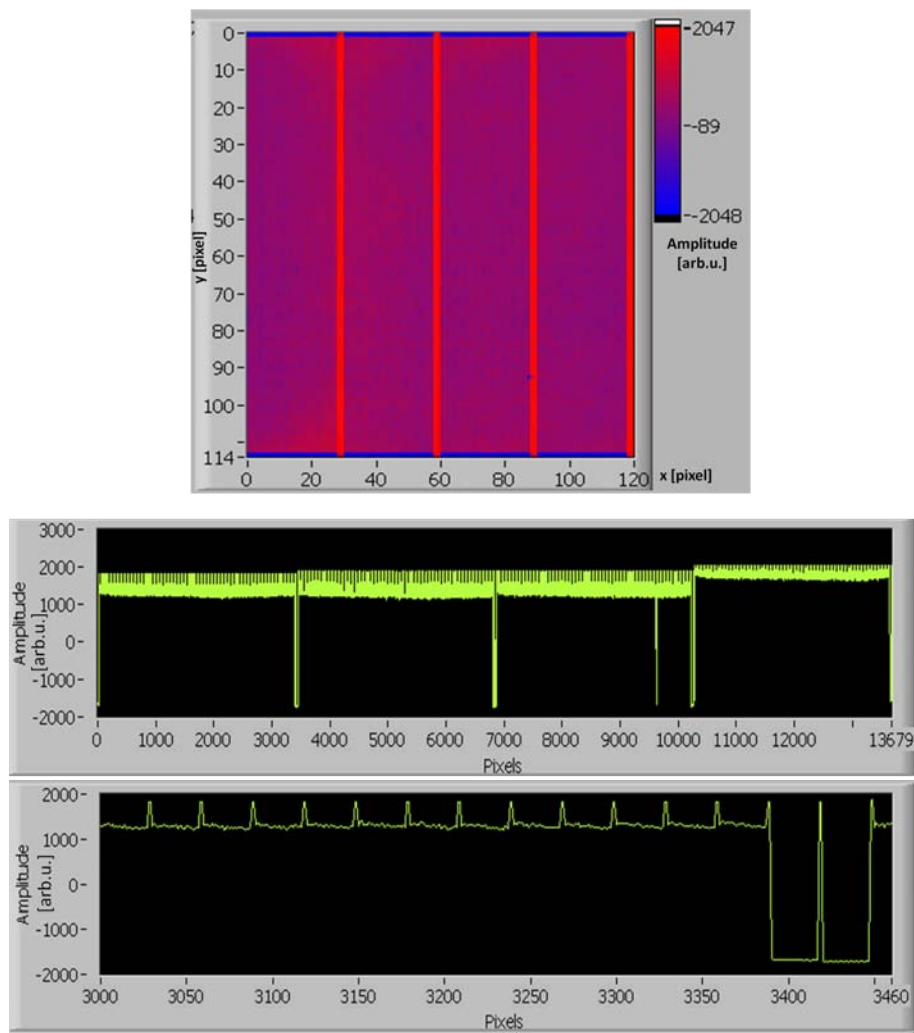


Figure 3.5: Visualization of the two-dimensional matrix with the marker pixels on the LabView front panel. Below the linear analog output of one readout frame.

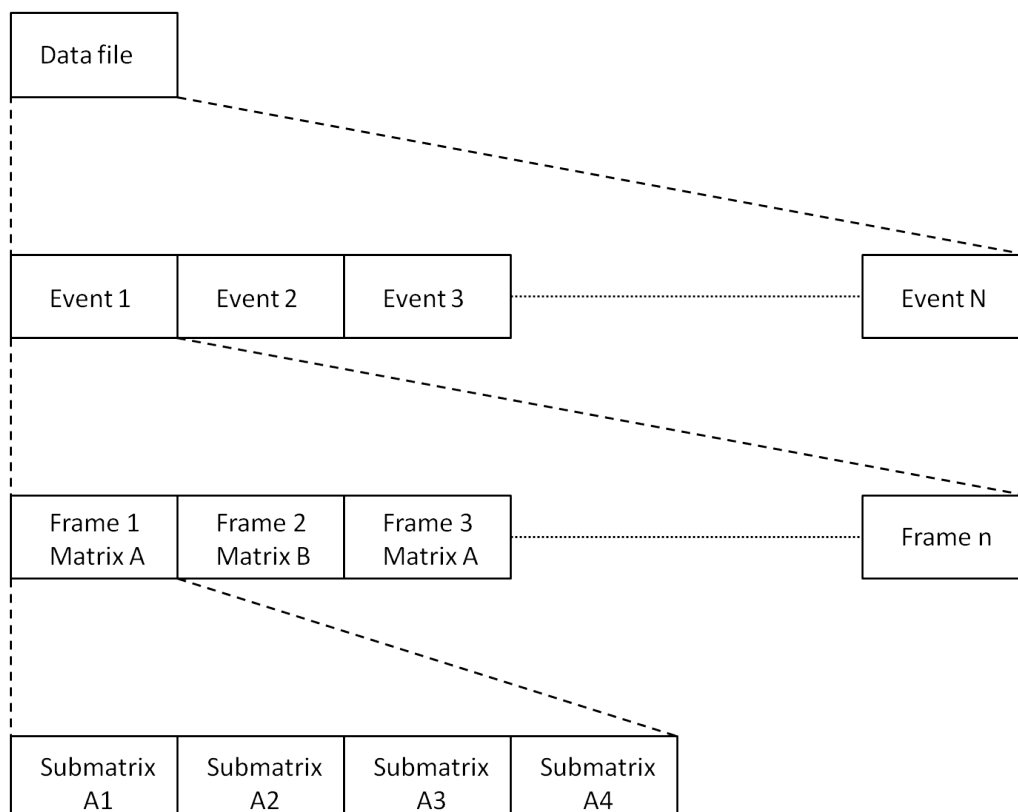


Figure 3.6: Structure of the data obtained from the Mimotera.

### 3.3 Data Analysis

There are two substantially different ways of dealing with the data files obtained from the Mimotera: The frame by frame imaging and the differential imaging.

#### Frame by Frame Imaging

Each of the readout frames is analyzed separately. The absolute pulse height of each pixel in the raw data file has to be corrected for pedestals, i.e. the time dependent background signal that is different for every pixel. This has to be done by taking an additional pedestal file containing only empty frames, preferably right before the actual measurement and subtracting the mean value for each pixel from the data file. The signal is normalized to the noise  $\nu$ , which is the standard deviation of the pedestal distribution, such that the final input value for the data analysis for each pixel is

$$S(n) = \frac{\text{pulse height}(n) - \overline{\text{pedestal}}}{\nu} \quad (3.1)$$

where  $n$  is the frame number. This calculation has to be performed for matrices A and B separately, as they are physically different and, therefore, have different pedestals and noise levels. This mode is useful for continuous signals, for example when imaging a laser spot.

**Advantages:** All values have the same polarity and details of the matrix structure are visible. For example the faulty pixel that is visible in Fig. 3.5 would disappear in an analysis with the differential mode.

**Disadvantage:** As mentioned above, it is necessary to keep exact track of the pedestals. This has to be done by taking additional data files, and even then there is a systematic error if the pedestal shifts in between the background measurement and the taking of the actual data. The pedestals can vary strongly with time, which is why a new method has been developed for the measurements at HIT, providing the possibility of tracking them more closely in time to the actual data. This will be described in chapter 5.

## Differential Imaging

In this mode, not the absolute signal, but the difference between two subsequent frames is considered. Taking into account the timing structure in Fig. 3.4, the difference is build for matrices A and B separately, such that for matrix A one gets frames 4-2, 6-4, 8-6, etc. and for matrix B frames 3-1, 5-3, 7-5, etc. The resulting signal for each pixel is

$$\Delta(n) = \text{pulse height}(n) - \text{pulse height}(n-2) \quad (3.2)$$

again, to be carried out separately for both matrices A and B.

**Advantage:** One does not need to consider the pedestals, as they can be expected to be the same for two subsequent frames. The difference is thus zero and they do not contribute to the signal. This method is very useful for the experimental conditions at ACE, where the beam is contained in only one readout frame, and thus the difference of two frames results in the absolute signal.

**Disadvantages:** The resulting signal can be either positive or negative, depending on the chronological order of the frames before subtraction. Details of the matrix structure, like dead pixels, get lost as they are the same in every frame.

## Analog versus Counting

Apart from the two different imaging modalities described above, there is another distinction one can make in the analysis of the data. One possibility is to take into consideration the absolute, analog pulse height in each pixel, the other one is to do particle counting. The Mimotera is able to do both. In the counting mode, a pixel can only be regarded as hit or not hit, the height of the signal is without relevance. This provides a direct measurement of the particle flux, without calibration. A threshold has to be defined beforehand, above which a pixel counts as being hit, below as being not hit. For this method it is important to reduce the crosstalk between neighboring pixels, in order not to count a particle twice. This is possible due to the multiple readout diodes in each pixel described in 3.1. The most important and severe limitation, however, is that it is not applicable in a pile-up situation, namely if the flux is so high that the mean number of particles per pixel per frame exceeds one. In this case, two particles in the same pixel in the same frame are only counted as one. Therefore this mode is only useful for low intensity beams.

The analog method on the other hand can still be used even if the experimental conditions lead to pile-up, as the absolute signal height for a monoenergetic beam depends only on the number of particles hitting the pixel. This is valid as long as the dynamic range of the detector is not completely exhausted and saturation is reached. This is a challenge at ACE, as will be seen in chapter 4. On the other hand, the analog method requires a calibration for a measurement of the absolute intensity, as otherwise it is not known how to interpret the pulse height of a signal. This calibration might even be time dependent.

At ACE there is definitely a situation of pile-up, as the intensity is  $3 \times 10^7$  particles in one frame and the Mimotera has only  $1.25 \times 10^4$  pixels. Therefore, the analog mode has to be used. Furthermore, it is convenient not to subtract the pedestals, especially because the spill of antiprotons is contained in only one readout frame and subtracting the pedestal is equal to simply subtracting the previous frame. This is the reason for choosing the differential imaging.

The analysis of the data is carried out with ROOT, a data analysis framework from CERN, [20] using different macros written in C.

## 3.4 Why the Mimotera is the System of Choice

### Thickness

The total thickness of the PCB system is about 2 mm. For the 126 MeV antiprotons at ACE with a range of approximately 10 cm in water, this does not disturb the operation significantly. The system is installed close to the water tank, so that the effect caused by multiple scattering in the air between sensor and the cell sample is negligible.

A Monte-Carlo-simulation has been performed with FLUKA, in order to compare the beam straggling caused by the Mimotera, the air and the water tank. The results can be seen in Fig. 3.7. Distance zero along the beam direction indicates the edge of the PMMA water tank, which has an entrance window of 3 mm thickness. In front of the tank, the Mimotera is mounted, both are surrounded by air. The additional straggling of the beam caused by the Mimotera is extremely small. The number of particles scattered by the system is of the order of only 0.01 % of the total number of particles in the beam. Moreover, for modifying the energy of the beam in several steps to produce a spread-out Bragg-peak, degraders of 1 mm of PMMA are inserted in the beam line in front of the Mimotera. This increases the beam straggling by far more, making it already necessary to account for it in the Monte Carlo dose calculations. Thus, for the energy range interesting for ACE, the Mimotera is thin enough not to disturb the operation significantly.

### Size

The active area of the Mimotera is only  $17 \times 17$  mm. Thus it is not possible to monitor beams with large diameters, for example de-focused clinical proton beams as used at HIT, see section 5.1. Nevertheless, as the antiproton beam at ACE has a FWHM of only about 7 mm, the Mimotera is large enough to monitor the whole beam spot.

### Position and Time Resolution

The spatial resolution of the sensor is  $153 \mu\text{m}$ . This is fully sufficient for the ACE requirements, because for a profile of 7 mm FWHM, about  $7 \text{ mm} / 153 \mu\text{m} = 45$  data points are obtained in the central region. Therefore, the pixel size of the Mimotera is small enough to provide a good profile measurement of the beam. The high frame rate of up to 10 kHz is not of major importance for the ACE set-up, but it will be important when monitoring continuous beams of protons and carbon ions at HIT, see chapter 5.

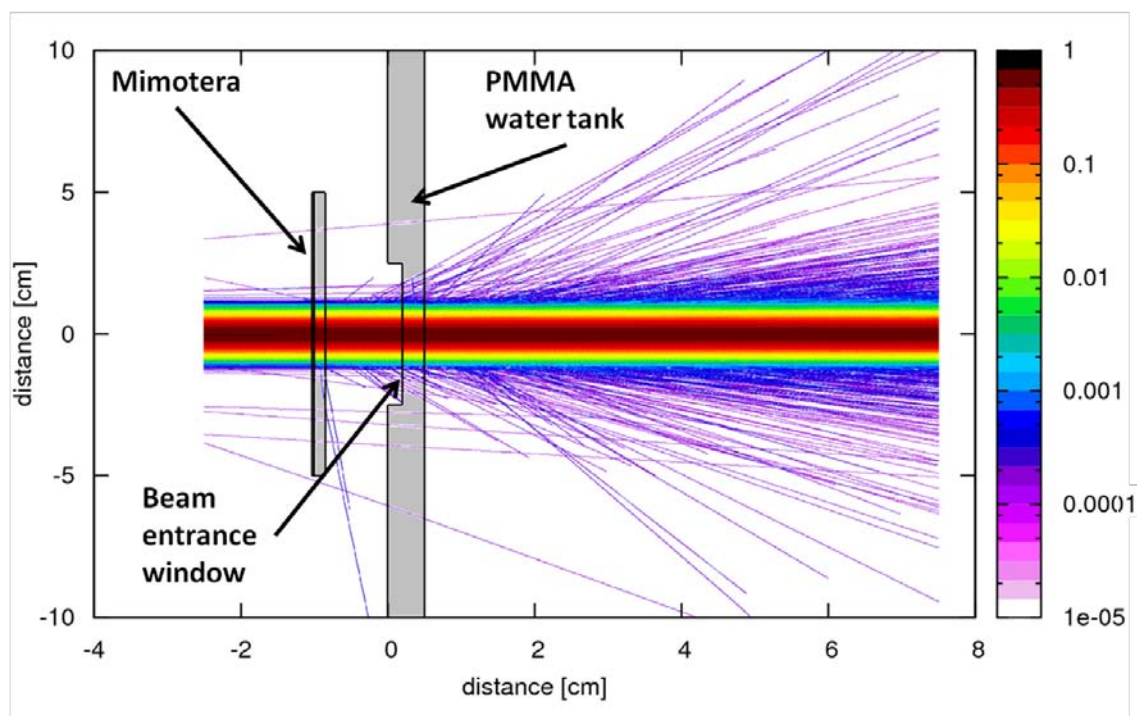


Figure 3.7: Simulation of beam straggling in ACE.

## Pixel layout

The fact that the Mimotera is a dead-time-free detector may not seem very important for ACE, as only single shots with a very low repetition rate need to be detected. Nevertheless, it influences the measurement due to the implemented read-out procedure of the Mimotera: It is not possible to trigger the timing sequence displayed in Fig 3.4 directly, the system is continuously integrating and reading out as explained above. Only the saving of the data in the internal buffer to a file can be triggered. Therefore, one can not start an integration frame manually, the trigger arrives randomly with respect to the timing structure of the Mimotera readout. This means that about one half of the spills are arriving in matrix A, the other half is read out in matrix B, thus it is necessary to consider both matrices in order not to lose any spills.

It is known from other beam monitoring systems like external scintillators, beam current monitor, etc. that the delay between the trigger pulse and the beam arrival is exactly  $4 \mu\text{s}$ . Therefore, the probability that the trigger arrives in one integration frame and the Mimotera data acquisition is already in the next frame when the actual beam spill arrives is negligible, as for an integration time of  $1.4 \text{ ms}$  it is of the order of  $4 \mu\text{s}/1.4 \text{ ms} = 3 \times 10^{-3}$ . Therefore, it is always known exactly which frame contains the beam image, but not which of the matrices is reading out this frame.

## Dynamic range

The electric potential in each pixel of the Mimotera is  $U = 2 \text{ V}$ , the capacitance can be chosen to be  $C = 0.5 \text{ pF}$  (called “attenuation off”) or  $5 \text{ pF}$  (called “attenuation on”), depending on which signal height is expected for a certain experimental set-up. As the particle flux at ACE is high in a short time interval, the larger capacitance is chosen. This means that every pixel can store a charge of up to  $Q = CU = 5 \text{ pF} \times 2 \text{ V} = 10^{-11} \text{ C}$ , which corresponds to  $10^{-11} \text{ C} / (1.6 \times 10^{-19} \text{ C}) = 6 \times 10^7$  electrons per pixel before reaching saturation. For the lower limit of charge carriers that can still be detected as a signal, one has to consider the equivalent noise charge of the sensor. [21] For the Mimotera this is about about 1000 electron-hole pairs per pixel. A signal to noise ratio of the order of 5 is desirable, therefore about  $5 \times 10^3$  electrons per pixel per frame are needed to obtain a stable and reliable signal.

The energy loss through ionization and excitation of a  $126 \text{ MeV}$  proton in the  $14 \mu\text{m}$  epi-layer in the Mimotera is  $16 \text{ keV}$ , see also section 5.3. [25] For an antiproton the energy loss can be considered to be equal, as for this energy the particles are far from being stopped in the volume, essentially no nuclear interactions take place and no annihilation events occur. The mean energy to create an electron-hole pair in silicon is  $3.62 \text{ eV}$  at room temperature, as stated in 2.2.1. This means that each antiproton on average sets free  $16 \text{ keV} / 3.62 \text{ eV} = 4.4 \times 10^3$  electrons when traversing the epi-layer of the Mimotera, which is safely above the mean noise level, such that single antiprotons could be detected. As a consequence, the upper limit of flux the Mimotera can handle is about  $6 \times 10^7 / (4.4 \times 10^3) = 1.4 \times 10^4$  antiprotons per pixel.

The number of antiprotons hitting one single pixel is highest in the center of the Gaussian and is calculated as follows: The probability that a particle hits the detector at  $-x_0 \leq x \leq x_0$ , is

$$P_x = \int_{x=-x_0}^{+x_0} \frac{1}{\sqrt{2\pi\sigma^2}} e^{-x^2/2\sigma^2} dx \quad (3.3)$$

with  $x_0 = 153 \mu\text{m} / 2 = 76.5 \mu\text{m}$  and  $\sigma = \text{FWHM} / 2\sqrt{2\ln 2} = 7 \text{ mm} / 2\sqrt{2\ln 2} = 2.97 \text{ mm}$ . An expansion leads to

$$e^{-x^2/2\sigma^2} = \sum_{i=0}^{\infty} \frac{(-x^2/2\sigma^2)^i}{i!} = \left(1 - \frac{x^2}{2\sigma^2} - \dots\right) = 1 \quad \text{for } x \ll \sigma \quad (3.4)$$

Inserting this in the integral above yields

$$P_x = \int_{x=-x_0}^{x_0} \frac{1}{\sqrt{2\pi\sigma^2}} dx = \frac{2x_0}{\sqrt{2\pi\sigma^2}} \quad (3.5)$$

As the distribution is symmetric, the probability of hitting the central pixel is

$$P = P_x \cdot P_y = \frac{(2x_0)^2}{2\pi\sigma^2} = \frac{(153 \mu\text{m})^2}{2\pi(2.97 \text{ mm})^2} = 4.2 \times 10^{-4} \quad (3.6)$$

which leads to a total number of particles in the central pixel of

$$N = P \cdot N_0 = 4.2 \times 10^{-4} \cdot 3 \times 10^7 = 1.3 \times 10^4 \quad (3.7)$$

for a total beam intensity of  $3 \times 10^7$  particles in one spill.

It has been calculated above that the Mimotera is able to cope with  $1.4 \times 10^4$  antiprotons per pixel with the attenuation turned on. Therefore, it can be expected that the sensor will be able to operate without saturation at ACE. The signal height seems to lie just barely below the upper limit of the dynamic range, but one has also to consider that the estimation above holds only for an ideal sensor that collects 100% of the charges generated in the active volume. This is of course not the case for any such device, several different effects reduce the charge collection efficiency. Three examples for such effects are:

A build-up effect similar to the situation with photons explained in section 1.1 has been observed also for carbon ions. It is of the order of some percent in a range of about 1 mm in PMMA. [22] The behavior of other ions like protons and antiprotons can be considered to be very similar. As the Mimotera has an entrance window of only about 100 nm and the epitaxial layer is as thin as  $14 \mu\text{m}$ , the signal does not reach its full height within the active volume. This reduces the number of generated charge carriers by a few percent.

A second effect that could reduce the signal height, is recombination of electron-hole pairs that annihilate before they are read out. Usually this effect can be neglected, [24] because the space charge region separates electrons and holes very quickly. Nevertheless, the Mimotera is a MAPS, in which no external voltage is applied to deplete the sensor, the charges are collected via thermal diffusion. Therefore, the lifetime of a signal charge could be a significant parameter. Measurements with ultra-thin silicon detectors in a 5 MeV antiproton beam have shown a significant reduction of the signal for lower bias voltages. [23]

Moreover, measurements at ACE have demonstrated that 15 readout cycles are not enough to collect all charge carriers generated in a single frame due to incomplete readout, see section 6.1. This reduces the height of the signal in the actual frame with the beam further, because a non-negligible fraction of the charges are collected only in the following frames.

In summary, the design of the Mimotera thus seems to be suitable for serving as a nearly-non-disturbing, direct beam monitor for the Antiproton Cell Experiment.

## 4 Antiproton Beam at ACE

### 4.1 The Challenge of Saturation

First tests of the application of the Mimotera as a beam monitor for ACE have been carried out in two and a half days of beam time in June 2010. The run was dedicated to detector testings, no cell samples were irradiated. The experimental set-up has been shown in Fig. 1.6. The Mimotera is mounted on a stand, 5 cm in front of the experiment. This holder was designed in such a way that it can be adjusted by 2 cm horizontally and vertically, to have the beam centered on the detector surface. The main purpose of this run was to investigate whether the Mimotera is operating without saturation at ACE, like the calculations of the energy loss in section 3.4 indicate. Three different systems have been tested regarding saturation effects, two on a PCB chip and one on a ceramic chip. The silicon sensor is the same in all three setups, but the electronics of PCB and CERAMIC differ, as stated in 3.1. The PCB2 sensor had a different pre-amplifier mounted in comparison to PCB1.

For a first overview, Figures 4.1 - 4.3 compare the three systems. As already explained in section 3.3, the data are analyzed differentially. The plots show the information saved in the frame containing the beam spill minus the previous frame of the same matrix without beam. In other words, the pictures correspond to the difference of signal minus noise, realized by subtraction of two single readout frames. They show one single beam spill, no averaging has been carried out. The left half of the plots displays the two-dimensional profile on the detector surface, as reconstructed from the one-dimensional data array. The right part is the corresponding one-dimensional projection of four rows of pixels along the mean value in x- or y-direction, respectively. For PCB2 and CERAMIC, a Gaussian fit has been performed with ROOT, the mean and sigma of the fit are shown on the projection.

At first glance it is obvious that the PCB1 detector is completely saturated in the central region. This design is certainly not applicable for the experimental situation given, therefore, PCB1 will in the following no longer be considered. The signal in PCB2 looks much better, although there is still a little flat top visible when comparing the profile to the Gaussian fit. A priori it is not clear, whether this behavior is due to saturation of the sensor or if the beam profile is not a pure Gaussian. The ceramic detector appears not to be saturated, which might indicate that the flat top in PCB2 is caused by saturation. The effect that is here referred to as “saturation” does not indicate that the dynamic range of the actual pixel is exceeded, as the silicon sensor is the same on all three boards. What is observed here

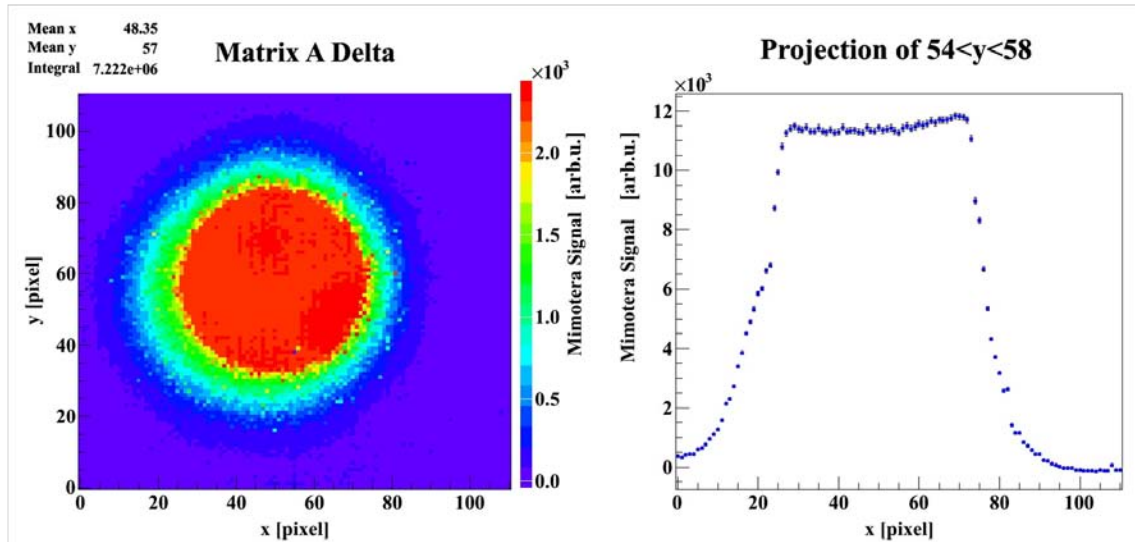


Figure 4.1: Profile PCB1.

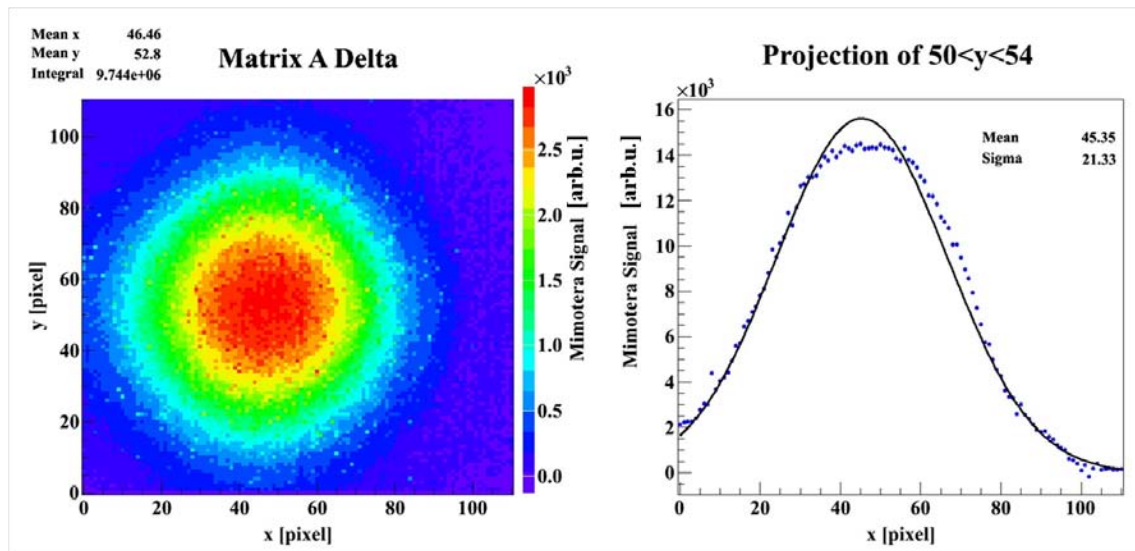


Figure 4.2: Profile PCB2.

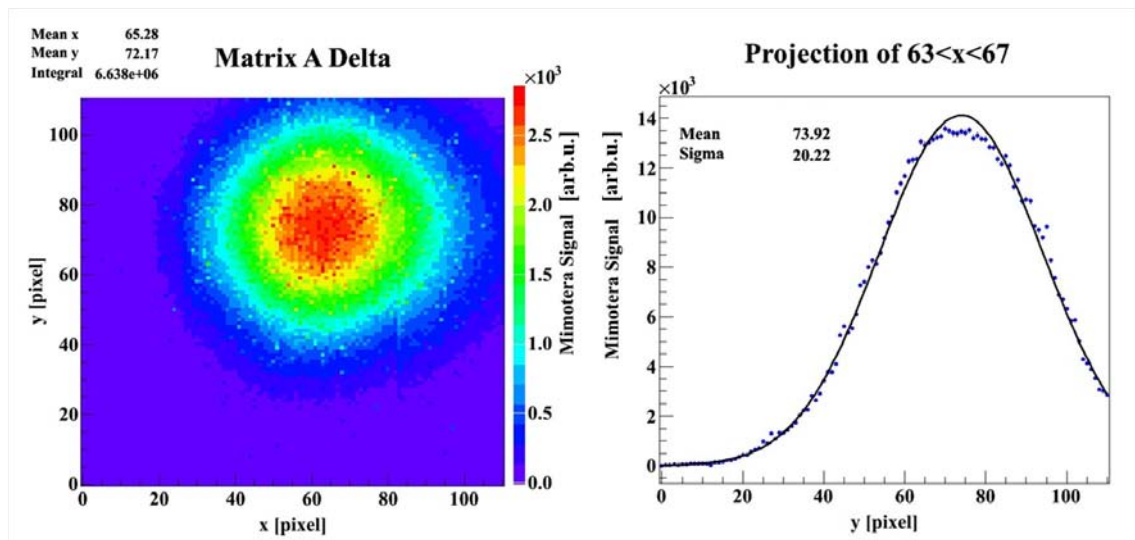


Figure 4.3: Profile CERAMIC.

is merely a saturation of the on-board electronics that can be reduced by exchanging the amplifier, as can be seen for PCB2.

To examine whether the PCB2 system is saturated in the beam core, Fig. 4.4 compares the integral of the detector signal as recorded with the PCB2 configuration to the corresponding beam intensity as provided by the beam control system of the accelerator. Each data point complies with one single spill. Fig. 4.4 shows different things: First of all it is obvious that the two readout matrices A and B behave differently in the sense that their signal height is different for the same beam intensity. This is not astonishing, as their respective electronics are physically different and operate independently from each other. The linear fit parameter  $p1$ , which indicates the slope, equals the calibration factor for transforming the signal in each matrix into the intensity. Secondly, the integral of the Mimotera signal seems to follow the beam intensity linearly. Although the variations in the intensity are usually not very large, fortunately there occurred two spills with a significantly reduced intensity in matrix A, which are very useful for this fit and confirm the good linear behavior. The slope is not decreasing with higher intensities, indicating that there is no saturation. However, the profile indicates saturation effects, when compared to the Gaussian fit, an assumption that seems reasonable. An additional gafchromic film also indicated a Gaussian shaped beam. This is why another approach has been used to investigate this question in more detail.

A region of interest (ROI) of the size of  $10 \times 10$  pixels in the beam core is chosen, and the same analysis is performed again. If the behavior of the sensor is really linear and there is no saturation of the pixels with highest intensity, then also their signal should increase linearly with increasing intensity. Looking at Fig. 4.5, it is obvious that this is indeed not the case. The signal in the ROI is no longer linear with the beam intensity. Compared to the two low-intensity spills, the slope decreases clearly for the high intensities.

Thus, the first impression obtained from the profiles projected was not false, a slight saturation for the typical intensity of the antiproton beam is experienced in the beam center. Nevertheless, the error resulting from this saturation is at most a few percent, which is of the same order of magnitude as reported for the other monitors used. Clearly it does not significantly affect the linear behavior of the integrated flux over the complete sensor, as the correlation in 4.4 shows. Thus, at this point it can be concluded that it is suitable to use the PCB2 system for monitoring the ACE beam. Unfortunately there was not enough beam time left to record an equally large data file to perform the same study for the ceramic system, as supposedly it would be linear also in the beam core.

Nevertheless, modifications have been made to the surrounding electronics on the chip to avoid the problem of saturation in the future also in the PCB detector. The operational amplifier has been exchanged, promising an operation of the system without saturation for the October beam time.

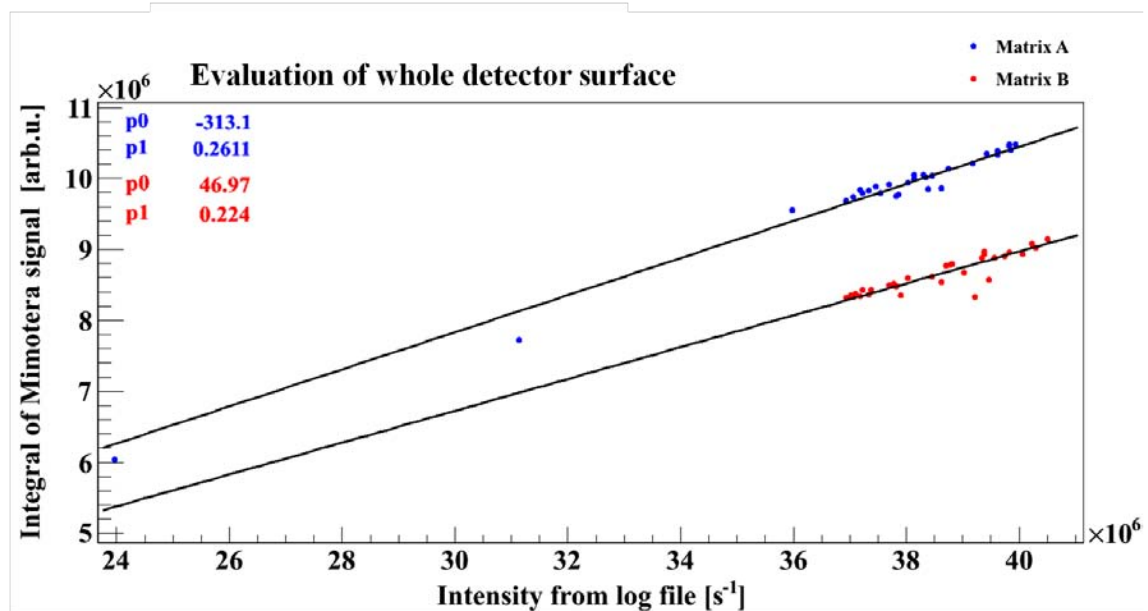


Figure 4.4: Correlation of PCB2 signal with intensity from log file.

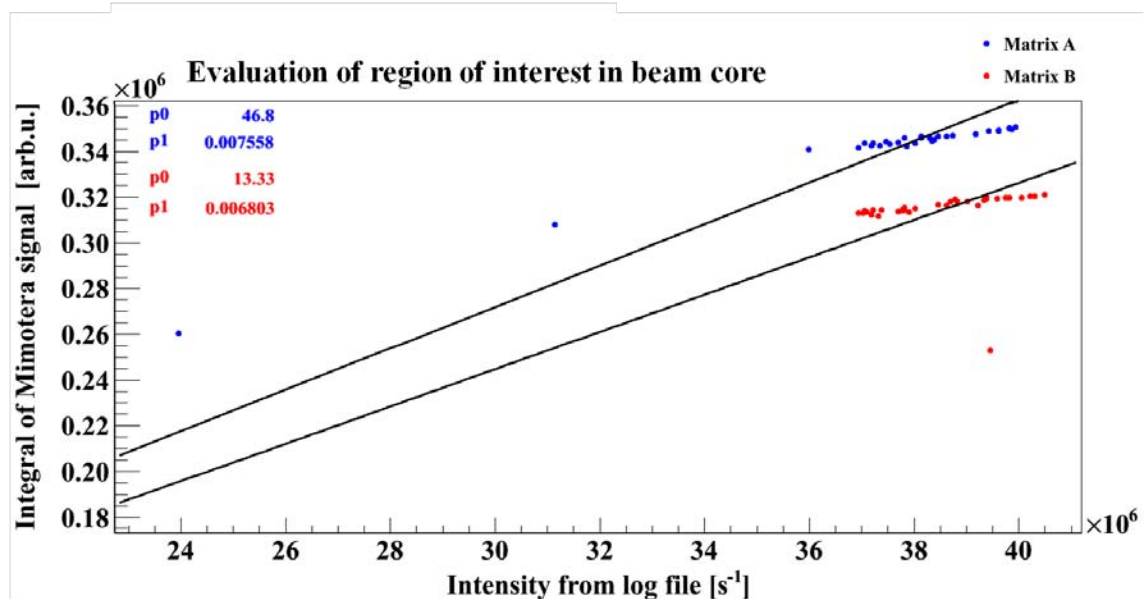


Figure 4.5: Correlation of PCB2 signal in ROI with intensity from log file. A linear fit to the data was forced to the origin for better visualization of the problem.

The same analysis as explained above has then been performed for a larger data file, taken with the PCB2 detector in October 2010. Fig. 4.6 corresponds to Fig. 4.4, Fig. 4.8 correlates with Fig. 4.5. The behavior of the sensor is now linear with increasing intensities, even in the core of the beam. Also, the relation of signal heights in matrix A and B changed with respect to the set-up in June: The two matrices are behaving nearly identical now, there is no longer a shift between their integrals.

Unfortunately, a different effect occurs for the October data: The linear fit in Fig. 4.6 and Fig. 4.8 does no longer cross zero. This is not the case when taking into account a ROI in the core of the beam, see Fig. 4.8. As the analysis is carried out differentially, this can not be a constant offset in the pixels because this would cancel out in the subtraction. It might be related to an effect that becomes visible when looking at the two-dimensional beam-profiles from the October run, one of which is shown in Fig. 4.9. There is a shift in the signal of one sub-quarter with respect to the neighboring one. This problem is caused by different baselines in each sub-quarter, as can be seen in the corresponding analog output of the matrix without beam in Fig. 4.10. The difference between the third and the fourth sub-matrix is largest, causing a discontinuity along the x-axis in the two-dimensional profile of each beam spill, see Fig. 4.9. This effect might have been already present in one of the sub-quarters in the set-up used in June, as indicated by Fig. 3.5. Nevertheless, it did not affect the profiles obtained in this run, because the beam was slightly shifted away from the center of the Mimotera, such that this particular sub-quarter was nearly not irradiated at all.

All efforts during the October beam time to eliminate these shifts failed, neither exchanging the cables, the DAQ board, or even the sensor itself, nor tuning the operation voltage on the DAQ board improved the situation substantially. Still, this constant offset should not disturb the differential analysis, and it is not yet understood why this effect is observed even after subtraction. This has to be investigated further for future beam times.

Nevertheless, the problem of saturation has been solved for the system used in the October run, as the correlation with the CERN log file is linear and as the amplitudes in Fig. 4.11 are below the saturation limit. The signal height of  $-2000$  arb.u. of the marker pixels indicates the maximum possible signal height in the sensor. Remember that the signal in the Mimotera is negative. The dynamic range is not fully exploited in this case. The estimation in section 3.4 indicated that the antiproton beam needs  $1.3/1.4 = 93\%$  of the dynamic range. Looking at Fig. 4.11, the signal seems to be smaller than this, leading to the conclusion that the signal is indeed somewhat reduced by the effects described in section 3.4.

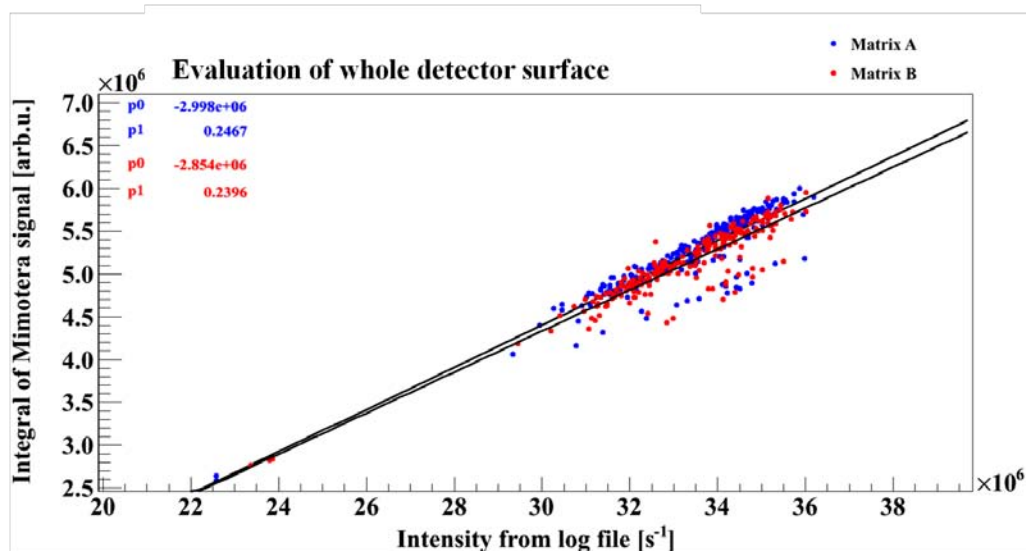


Figure 4.6: Integral taken over the whole detector surface compared to log file.

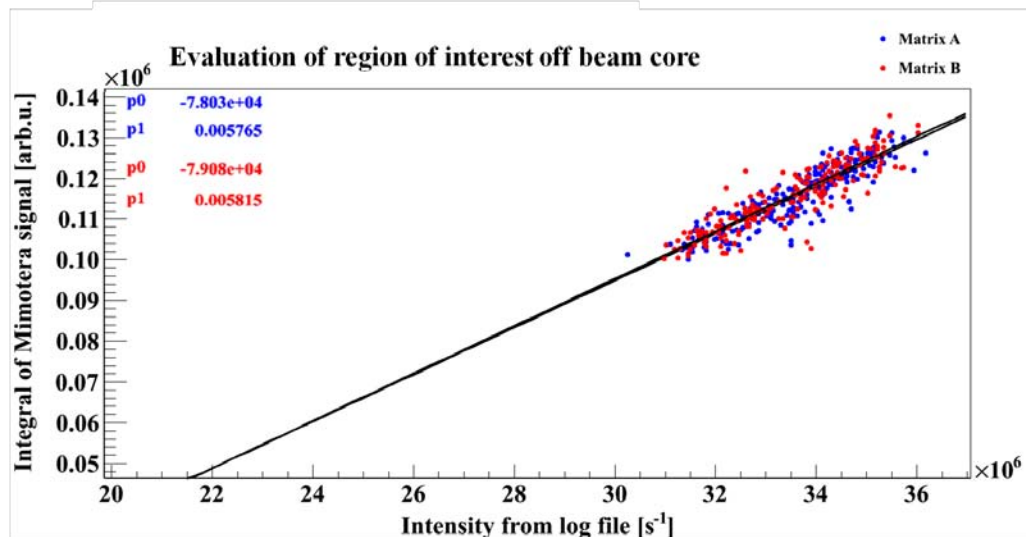


Figure 4.7: Integral in a ROI off the beam center compared to log file.

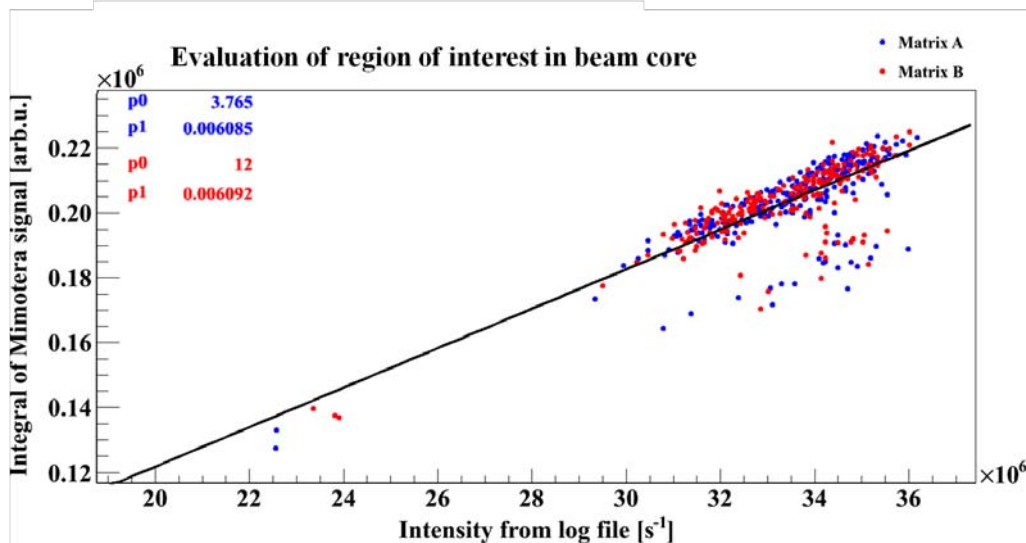


Figure 4.8: Integral in a ROI in the beam center compared to log file.

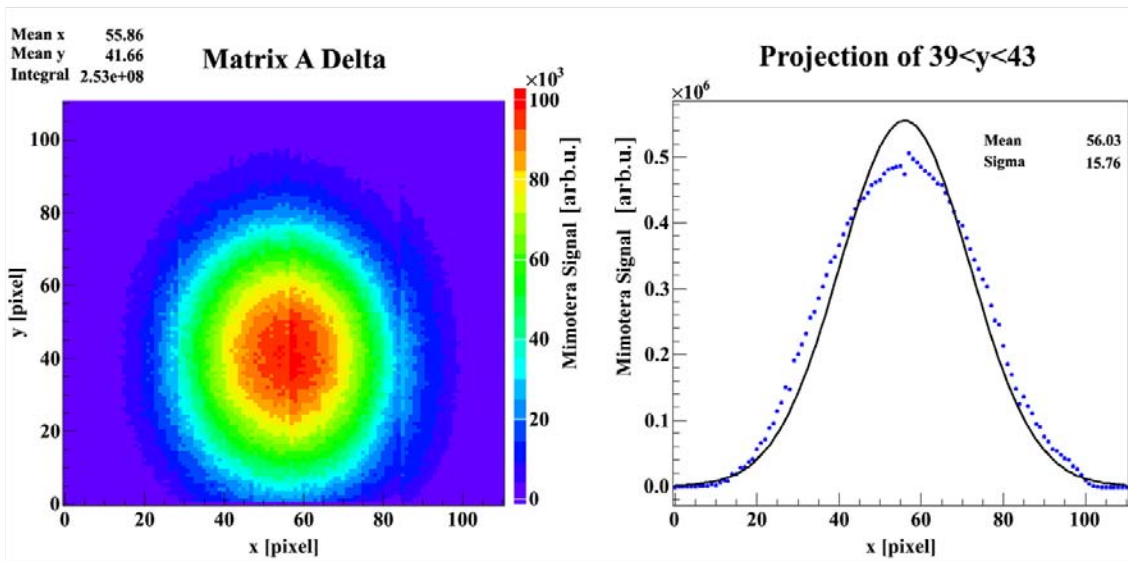


Figure 4.9: Profile in the Mimotera in the October run. For reasons of better visualization, 100 spills have been integrated.

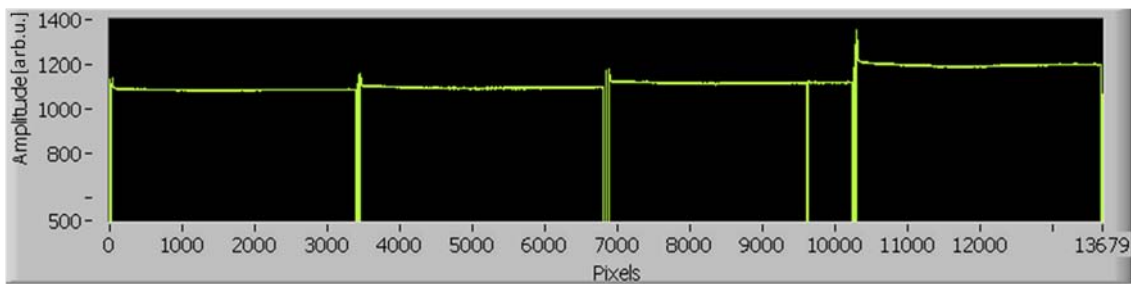


Figure 4.10: Analog output of matrix A of the Mimotera without signal (zoomed).

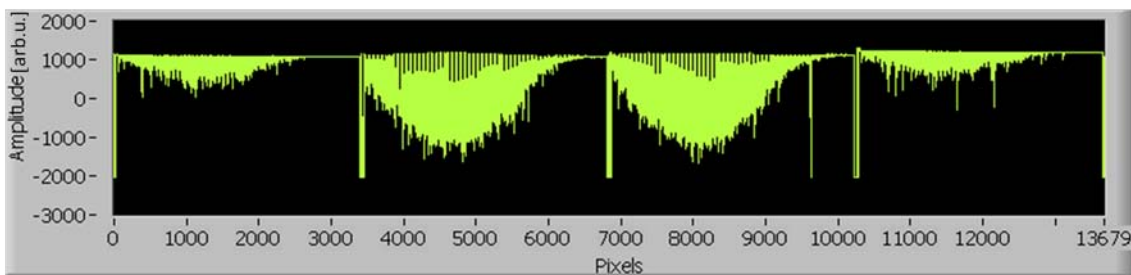


Figure 4.11: Analog output of matrix A of the Mimotera with signal.

## 4.2 Beam Monitoring

As stated in section 1.3, the future beam monitor for ACE shall provide a real-time, digital image of the beam profile and it shall track the fluctuations in beam intensity and position. The data analysis is performed in a way that all three quantities can be obtained quickly for each data file. For the beam profile, the two-dimensional plots along with projections in x- and y- directions are saved for every single shot, and one example is given in Fig. 4.12. Note that the data is taken from the PCB2 system in June, and therefore the small saturation effect is still visible.

For a real-time, online image of the beam, a two-dimensional beam profile and projections in x- and y-directions have also been implemented on the LabView front panel. This offers the possibility to recognize and correct a sudden change in profile or position of the beam within only one shot, as can be seen in Fig 4.13, taken on October 24, 2010. The cell sample can be removed from the water tank immediately, until the beam has been re-adjusted, and thus incorrect irradiation of the cell sample by more than one spill can be avoided. Using only a gafchromic film, this change would have been realized only after a long time, if at all, and the cell sample would have been totally lost for the data set.

The progression of the beam intensity is displayed by plotting the integral of the Mimotera signal for a consecutive spill number, see Fig. 4.14. In order to investigate the reliability of the accelerator log and the ionization chamber signals, their corresponding measurements are plotted as well. All are normalized to their integral over the spill number to fit on the same scale. In general, the course of the Mimotera signal follows the intensity of the log file very well. It seems to be at least as accurate in tracking relative changes of the beam intensity from shot to shot as the calibrated ionization chamber, and thus can be used to monitor the intensity fluctuations during an irradiation. This will allow to correct for occasional readout errors observed to occur for the ionization chamber, caused by trigger problems of the main control software of the experiment, as for example for spills 31, 32, 59 and 60. For spills 36–40, the signals of the Mimotera and of the ionization chamber lie on top of each other.

The two-dimensional beam position is defined by the mean values of the beam profile in x- and y-directions respectively, and is tracked in a similar plot. It is usually very stable, with maximum fluctuations of less than two pixels ( $300\ \mu\text{m}$ ) along the x-, and even less, about one pixel along the y-direction. Nevertheless, in October a situation occurred that demonstrated the major improvement that the Mimotera offers for ACE. Fig. 4.15 shows the position tracking over a period of 14 hours of beam time. There was a sudden, large change in the beam position at spill number 517 that would have been disastrous for the cell irradiation, if unnoticed.

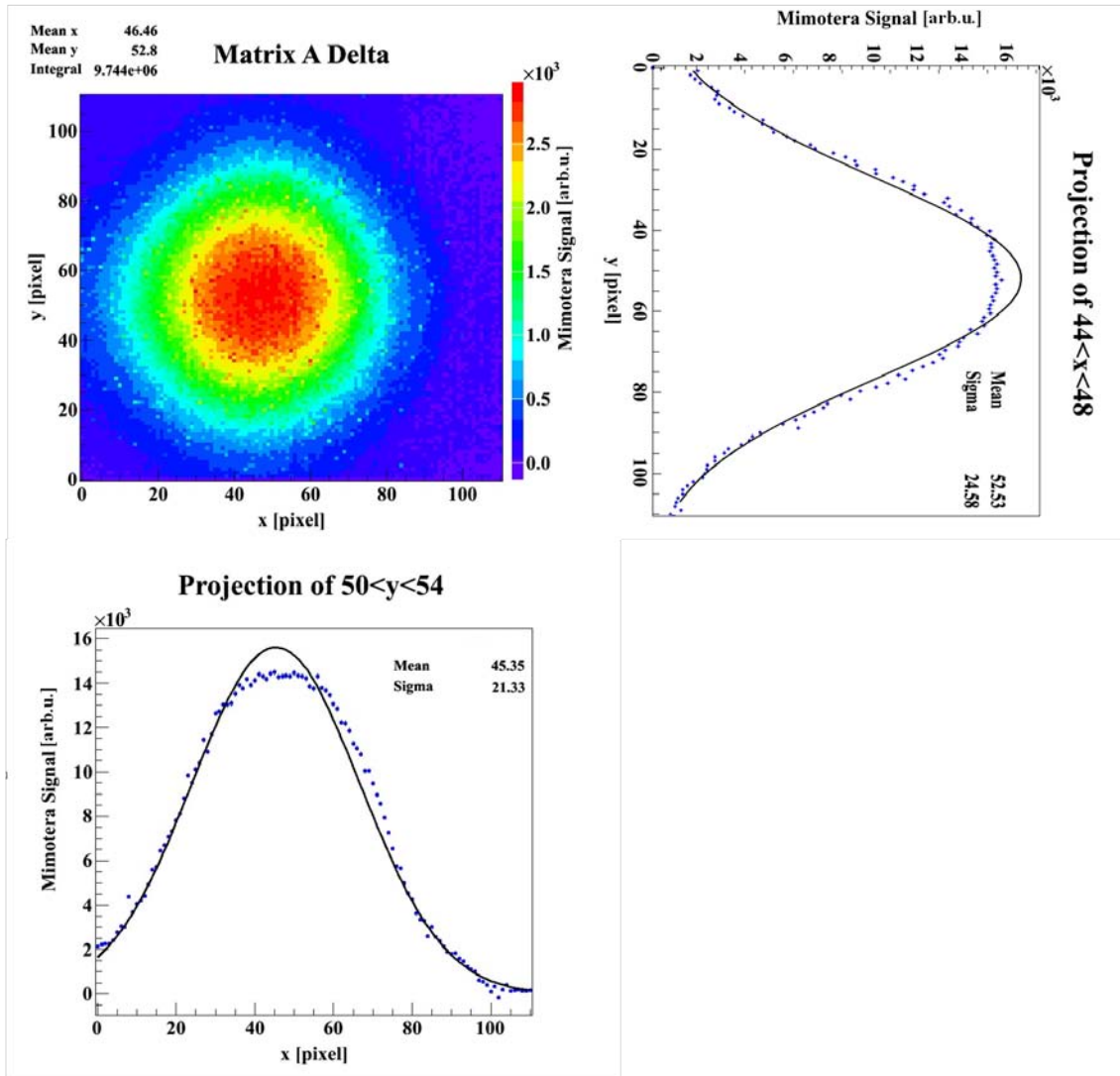


Figure 4.12: Monitoring the beam profile for every single shot of antiprotons with the Mimotera.

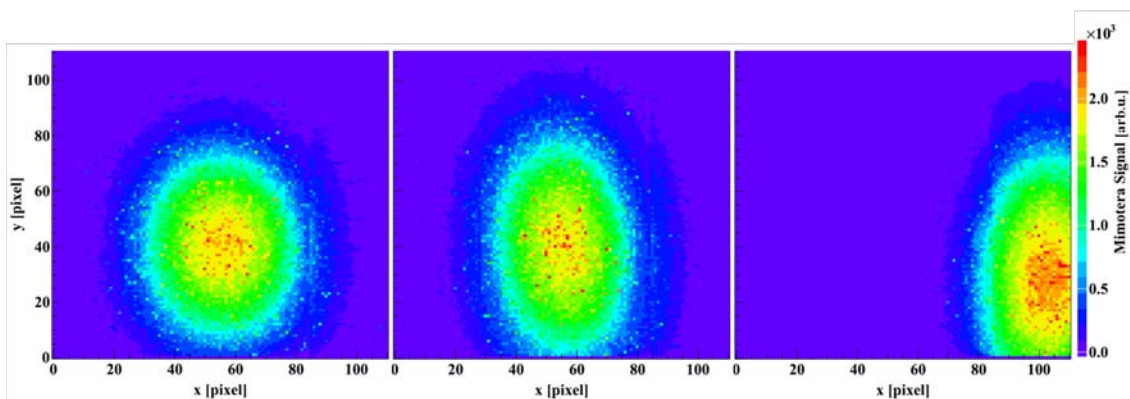


Figure 4.13: Three beam profiles recorded on October 24, 2010. There is a clear change in shape and position of the beam.

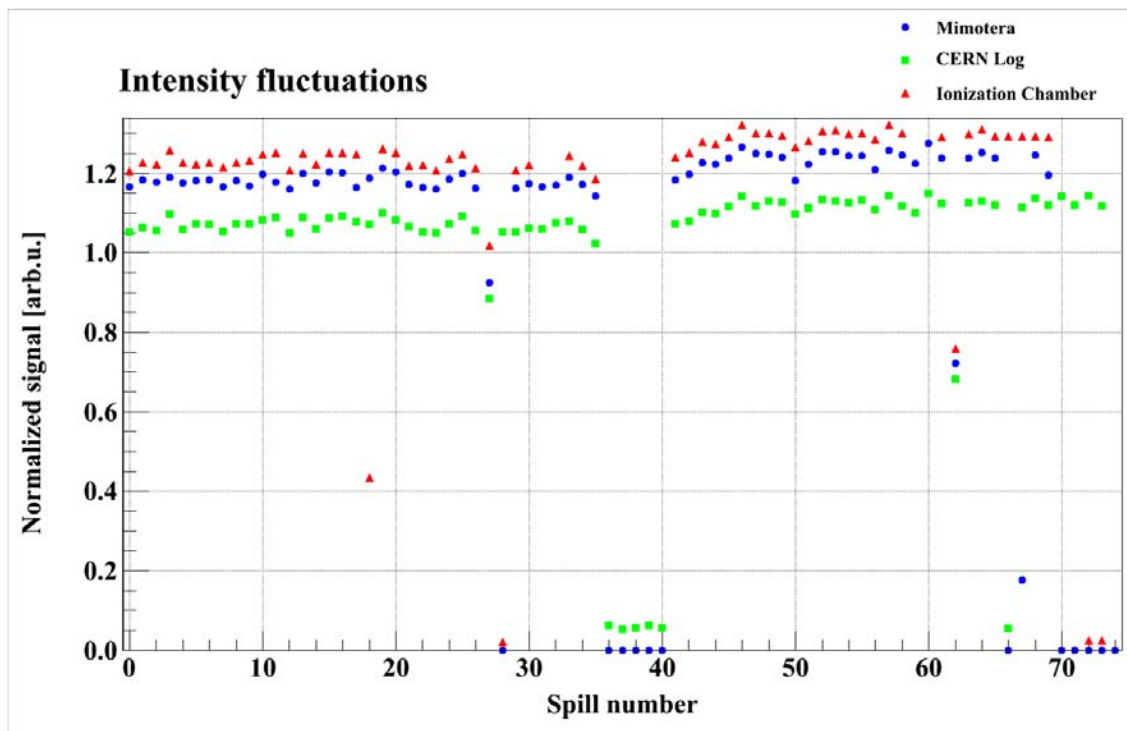
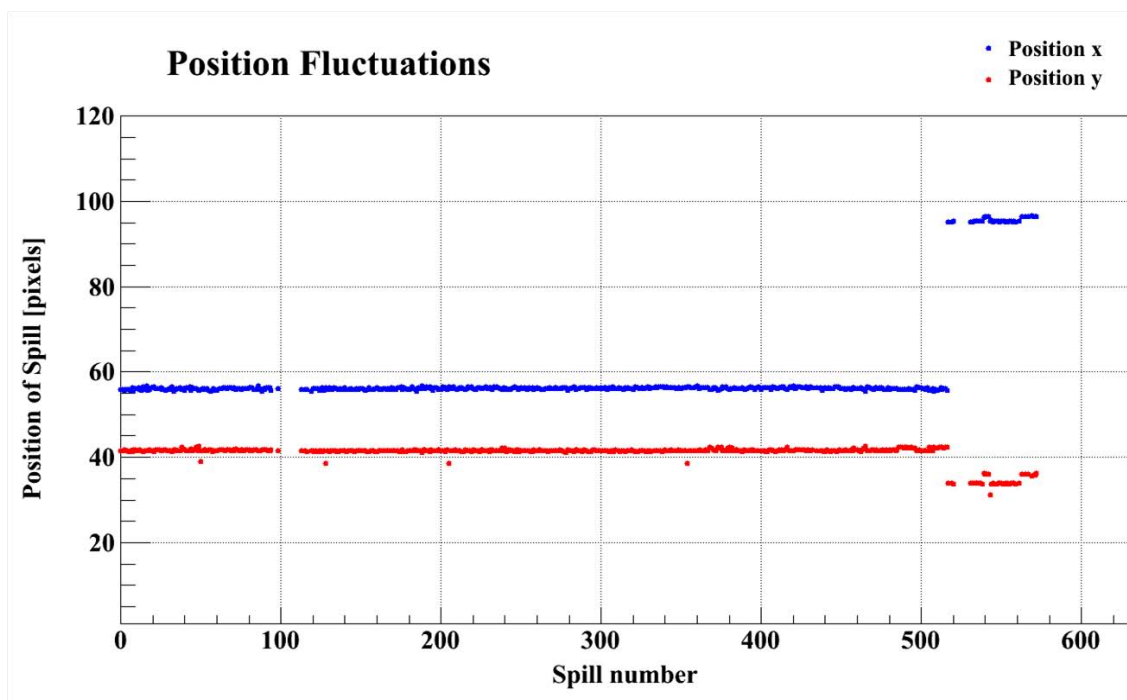


Figure 4.14: Tracking the intensity fluctuations during 110 min of beam time (70 shots) with the Mimotera.



## 4.3 The Mimotera as an Alignment Tool

The Mimotera proved to be an excellent choice not only for the tracking of the beam intensity and position, but also for substantially improving the initial alignment procedure of the beam during the preparation of the experiment. The front panel of the LabView interface for the data acquisition provides an online image of the beam that can be accessed from the accelerator control room via remote desktop connection. A wrong position or beam shape can be corrected by re-adjusting the dipole and quadrupole magnets in the ACE beam line within only a few shots. This has been impossible with the previous set-up, using gafchromic films which need about half an hour of exposure followed by a time consuming scanning routine until the beam position and shape are obtained.

It is also possible to not only direct the beam to the center of the Mimotera, but furthermore to align the experimental table to the beam. For this purpose, a second Mimotera has been placed approximately 50 cm behind the first one. The water tank in the middle is removed and the beam travels through air. Simulations with FLUKA have shown that despite straggling caused by the first Mimotera and the 50 cm of air in between the two detectors, it should still be possible to observe a fairly good beam profile, and thus to verify the alignment, as can be seen in Fig 4.16

The profiles that were obtained on the Mimotera in front of and behind the experiment respectively, are shown in Fig. 4.17, along with their corresponding projections in Fig 4.18. The results agree very well with the simulations and it is easily possible to determine the center of the beam profile on the second Mimotera. In the case illustrated, the mean value of the distribution differs only by about 4 pixels in x- and 3 pixels in y-direction over the range of 50 cm, which corresponds to an angle of  $\arctan[3 \times 153 \mu\text{m}/50 \text{ cm}] = 0.056$  degrees. The rear Mimotera is also mounted on an adjustable holder, such that it can be moved to achieve an image of the beam centered on the detector. Afterwards the Mimotera chip is removed from the holder, to allow a laser beam to be aligned to the center of the front and rear Mimotera. Subsequently, the water tank is adjusted to be precisely in line with the laser and, thus also with the antiproton beam.

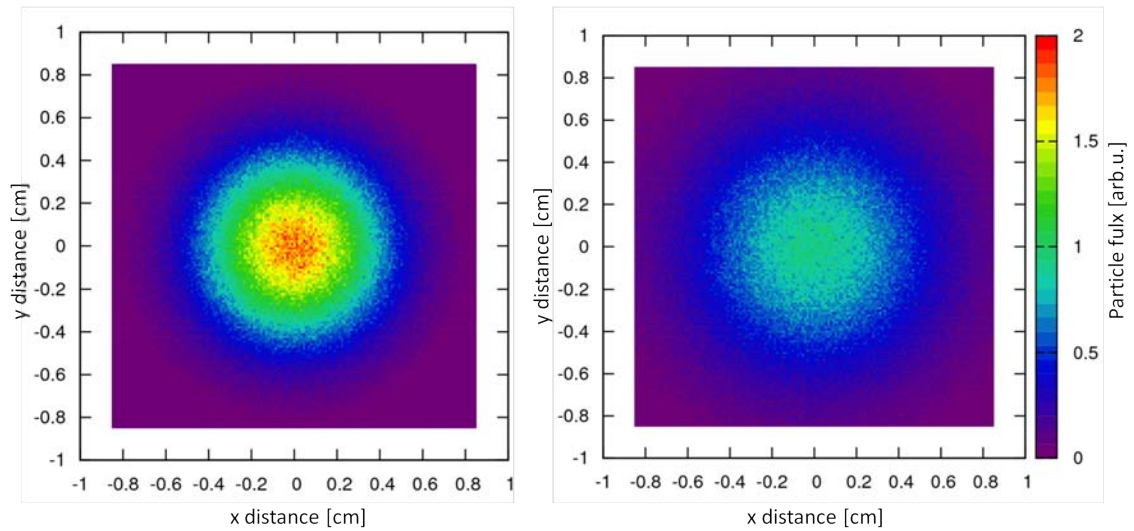


Figure 4.16: Simulated signal in the front and the rear Mimotera.

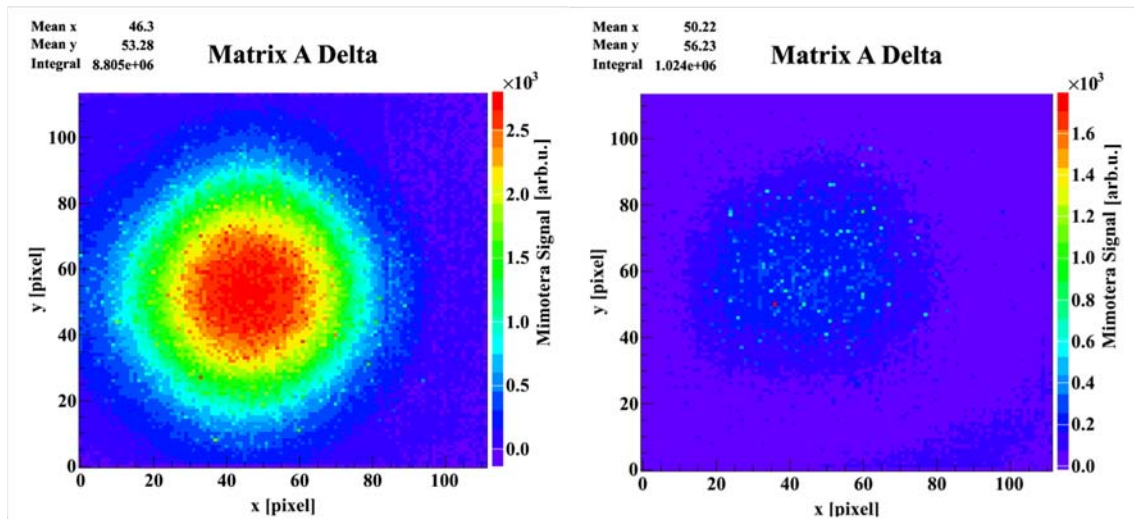


Figure 4.17: Measured profiles on the front and rear Mimotera.

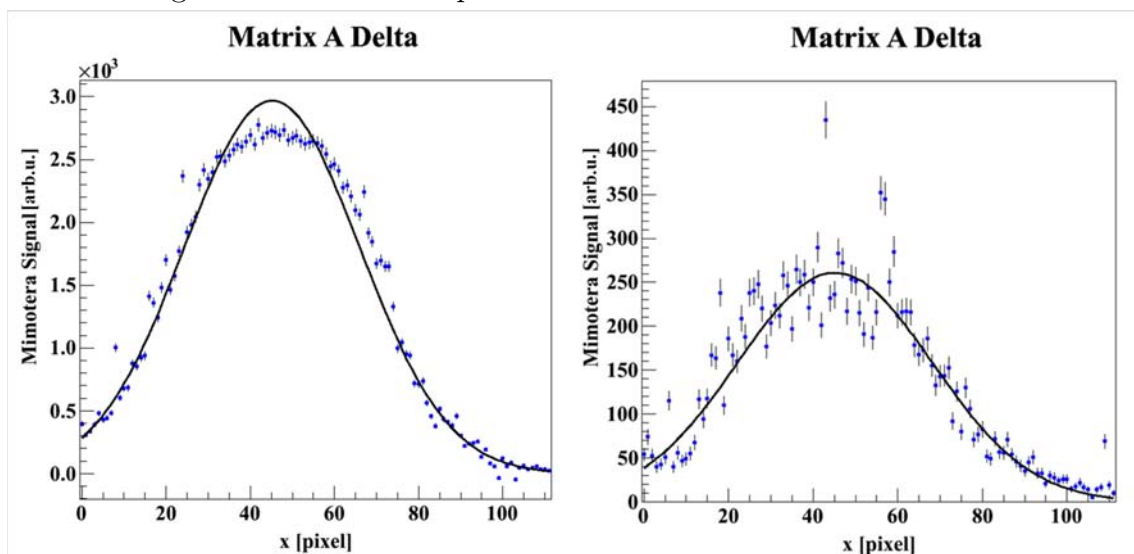


Figure 4.18: Projections corresponding to Fig. 4.17.

## 5 Ion Beams at HIT

Having demonstrated the suitability of the Mimotera for monitoring antiproton beams, which may be used for cancer treatment only in the not-so-near future, if at all, it is tempting to test the chip also for more conventional ion beams. The most commonly used hadrons for cancer therapy are protons and carbon ions. Both are applied at the Heidelberg Ion-Beam Therapy Center (HIT), where the experiments described below have been carried out. The irradiations took place in the quality assurance room of the facility, during the breaks in between the patient treatments.

### 5.1 Experimental Conditions at HIT

The timing structure of the beam at HIT is such that every spill of ions is five seconds long, followed by a five second intermission. In Tab. 5.1 the beam characteristics are listed as provided by the accelerator operation system.

Properties	Protons	Carbon ions
$E_{min}$ [MeV/u]	48.12	88.83
$E_{max}$ [MeV/u]	221.06	430.10
Energy steps	255 steps, 1mm in depth each	
$FWHM_{min}$ [mm]	8.1 - 12.6*	3.4 - 9.8*
$FWHM_{max}$ [mm]	32.4 - 32.7*	9.8 - 13.4*
Focus steps	4 steps	
$I_{min}$ [s <sup>-1</sup> ]	$2.0 \times 10^8$	$5.0 \times 10^6$
$I_{max}$ [s <sup>-1</sup> ]	$3.2 \times 10^9$	$8.0 \times 10^7$
Intensity steps	8 steps	

Table 5.1: Beam characteristics at HIT.

\* Smaller values correspond to higher energies

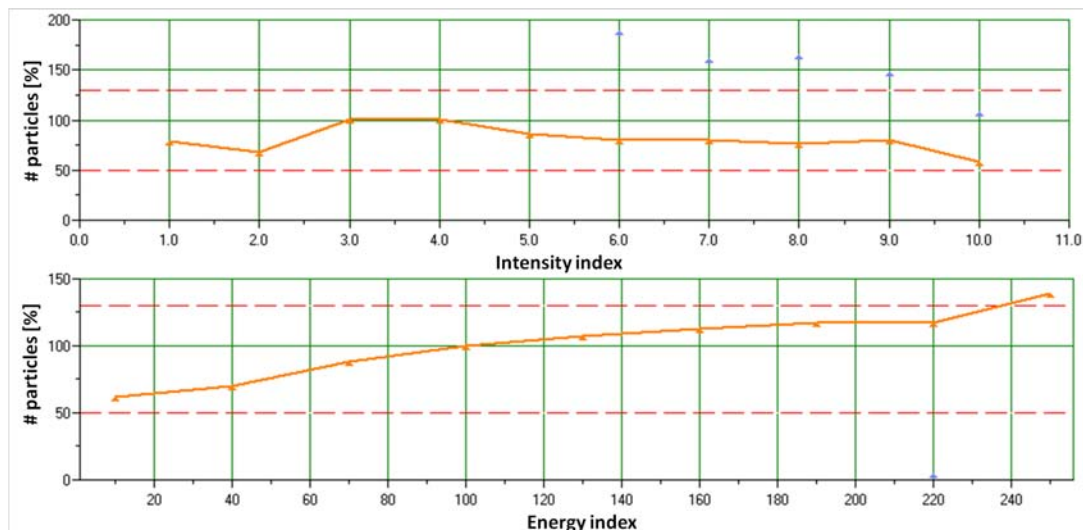


Figure 5.1: Result of the daily quality assurance measurement for carbon ion beams at HIT from October 7, 2010. Intensity steps 1 and 2 are not available for treatment yet.

Unfortunately, there are some technical issues at HIT, which make the analysis of the data a bit more complicated. First, the intensity steps mentioned above are not stable, but change from day to day and possibly even during the day. Therefore, one has to take into account the results of the daily quality assurance tests in the morning. A result may look like Fig. 5.1, taken on October 7, 2010. The vertical axis in both the upper and the lower panel displays the deviations of the measured number of particles from the nominal beam intensity in percent. 100% corresponds to a measured value equal to the expected value. These deviations depend on the intensity step chosen, as shown in the upper plot, and also on the beam energy, illustrated in the lower plot of Fig. 5.1. The variations are rather big, they reach up to  $\pm 50\%$ . The reference value of the intensity thus has to be corrected with the help of these graphs. It is calculated as nominal intensity  $\times$  intensity correction factor  $\times$  energy correction factor. Nevertheless, this method is not very exact, as the measurements are not only done just once per day, they are currently also not provided to the users in digital form.

Moreover, the intensity is not at all stable during one beam spill. It fluctuates in a wide range of about  $\pm 30\%$  around the mean value, as will be seen from the Mimotera signal in the next section. There is no internal tracking of these fluctuations, only the total number of particles delivered to a certain point in the position-space is controlled, as this is the only quantity necessary to assure that the treatment plan is followed precisely. As soon as the prescribed number is reached, the spill is aborted and the treatment moves to the next position.

## 5.2 Carbon Ions

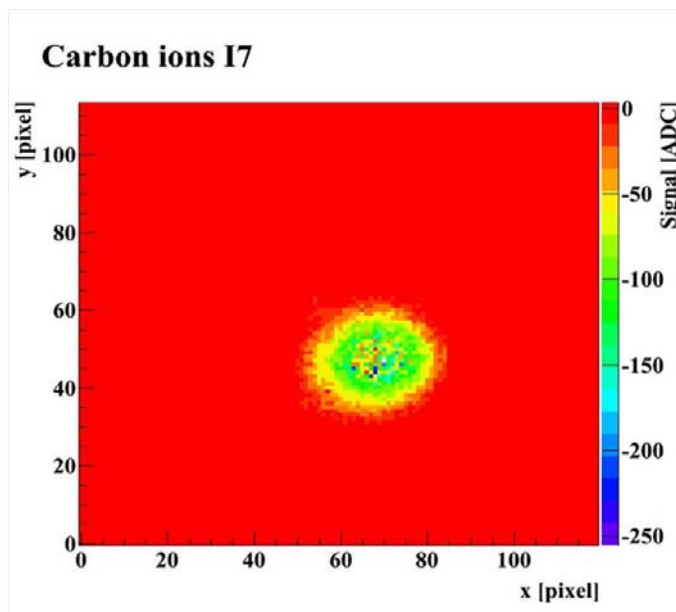


Figure 5.2: Profile of a carbon beam of intensity step 7 on the Mimotera.

The PCB2 Mimotera, with the same modified electronics as in the ACE run in October 2010, but with the attenuation turned off, was placed directly in a carbon ion beam and a scan of all eight currently available intensity steps has been carried out. One of the beam spots can be seen in Fig. 5.2. For each step, the irradiation plan was about two minutes long, resulting in an effective irradiation time of one minute. The energy of the carbon ions was chosen to be 409.97 MeV/u, because at this energy the smallest focus size of 3.4 mm FWHM is available. The nominal intensity was scanned from  $5.0 \times 10^6 \text{ s}^{-1}$  to  $8.0 \times 10^7 \text{ s}^{-1}$  in eight steps. The data was taken in a continuous mode, although not every frame can be saved to the file due to bandwidth limitations of the PC, as explained in 3.2.

Fig. 5.3 shows the raw data in the Mimotera. A region of interest of the size of  $40 \times 40$  pixels in the beam core has been chosen and the mean signal height in the ROI is plotted on the y-axis. Remember that the signal in the Mimotera is negative. The x-axis shows a progressive event number. A look at the analog amplitudes in Fig 5.4 explains the absolute numbers on the y-axis: The baseline of a pixel without signal lies above zero. If the beam is on, the (negative) signal in the Mimotera decreases from this reference value, as can be seen in pixels 7500–8700. This results in a total value of around 300 arb.u. for the signal with beam. The dynamic range is far from being saturated for the continuous carbon ion beam. This data has been taken without attenuation.

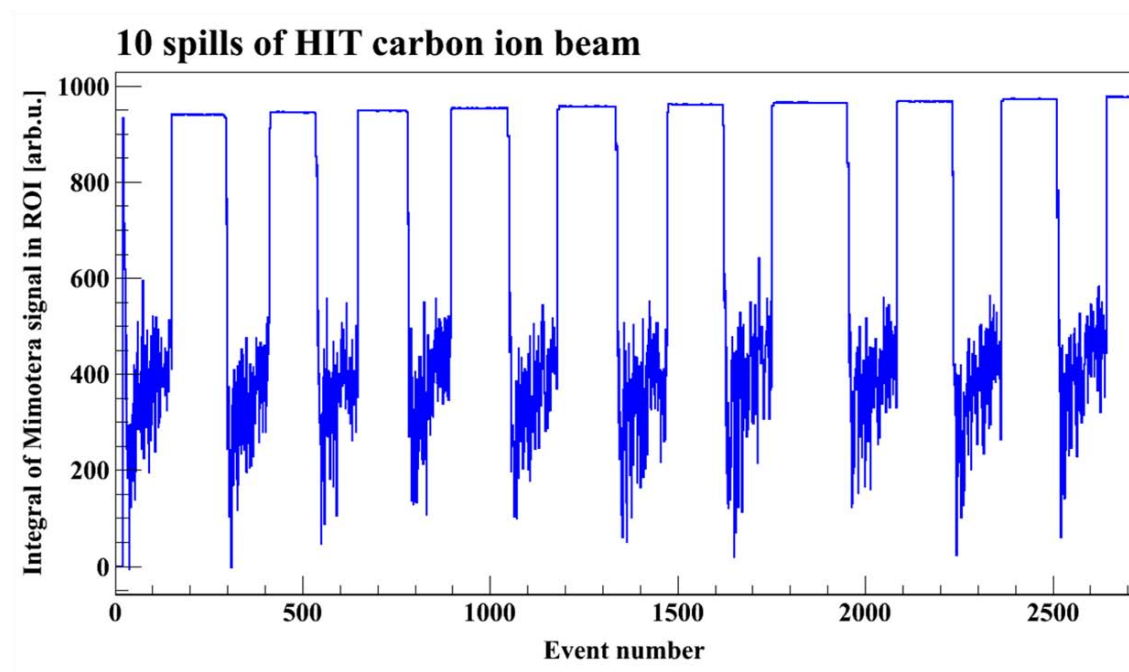


Figure 5.3: Spill structure of a carbon ion beam at HIT as measured by the Mimotera. The length of each spill is 5 s. Lower y-values correspond to a higher signal in the detector. The fluctuations during one spill go up to  $\pm 30\%$ .

By looking at Fig. 5.5, it becomes clear that the background signal in between two spills changes during time. Although the relative deviation in this time interval is only about  $40/1000 = 4\%$ , the time dependence of this drift is not known, and it did not seem suitable to just subtract the mean value of a separate pedestal file recorded beforehand, as it is usually done for the frame by frame imaging, see section 3.3. Instead, a routine has been developed that allows to subtract a time-dependent pedestal obtained from the beam intermissions that are anyway present in the data file. Therefore, the events have to be labeled automatically as with or without beam, to distinguish signal from pedestal. Each file has been started in a situation where the beam was off. The mean value of the first 20 frames is calculated and then taken as the mean pedestal height. If a threshold of five times sigma of this background signal is then exceeded by 20 frames in a row, the frames are considered to contain a beam spill. The same holds for the end of the spill: if the signal is lower than five times sigma of the mean signal with beam, 20 times in a row, then the beam is labeled as off. This procedure is repeated separately for every spill.

The main purpose of this experiment was to investigate the linearity of the Mimotera signal as a function of beam intensity, which is crucial for the operation at ACE as well as for possible applications of the Mimotera as a quality assurance tool for clinical therapy centers. At the beginning of this thesis, the intensity dependency

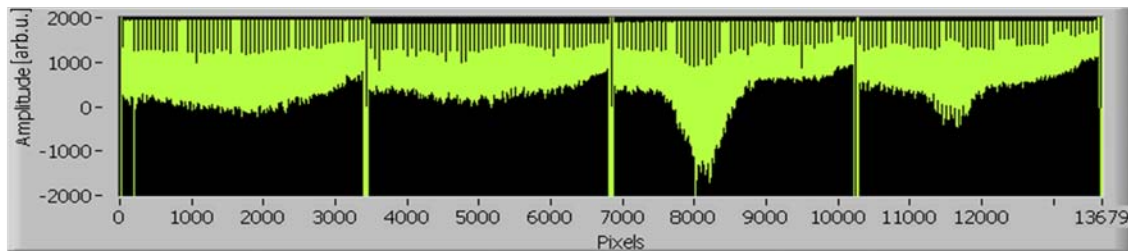


Figure 5.4: Analog output of the carbon ion beam in the Mimotera.

of the signal height in the detector had only been tested with a laser beam, with very good results, but for beam monitoring further analysis with particle beams was needed. At HIT it was possible to scan the intensity of the carbon beam in a wide range, which makes the results much more reliable than the measurements at ACE, where the largest deviation from the nominal intensity was an occasional reduction of about 40% of the maximum, see Fig 4.6.

The results of the analysis of the carbon data can be seen in Fig. 5.6. The mean value of all beam-on-events for a given intensity step minus the mean value of the corresponding beam-off-events is plotted on the y-axis. On the x-axis the nominal beam intensity at HIT is displayed, corrected by the factors according to Fig. 5.1. The plot in Fig. 5.6 shows that the signal is very well linear for different beam intensities. For the highest intensity of  $8 \times 10^7 \text{ s}^{-1}$ , which is not used in patient treatment, the accelerator operation is very unstable, and thus this data point cannot be considered reliable. The measurement confirms the good linearity of the Mimotera as a function of increasing beam intensity that has been observed already at ACE.

An additional measurement has been carried out to investigate the dependency of the signal in the Mimotera on the energy of the particles. This had never before been tested for this detector. The results can be seen in Fig 5.7. The signal in the Mimotera is evaluated in the same manner as for the intensity scan described above. The x-axis displays the energy loss of an ion in the Mimotera calculated with `bbt`. [25] Higher ion energies have a lower energy loss, see Bethe-equation in section 1.1. The energy has been scanned in a range between 150 MeV/n and 400 MeV/n. The behavior is very well linear.

Considering these results, it is reasonable to claim that the Mimotera could be a useful tool not only for the Antiproton Cell Experiment, but also to improve the daily quality assurance in clinical therapy centers like HIT. In the future it might even be possible to modify its design in a way that the detector could be implemented in the beam line permanently, to monitor the beam during irradiation. For this the backing behind the sensor would need further thinning and it would be preferable to increase its area by integrating four sensors on one chip.

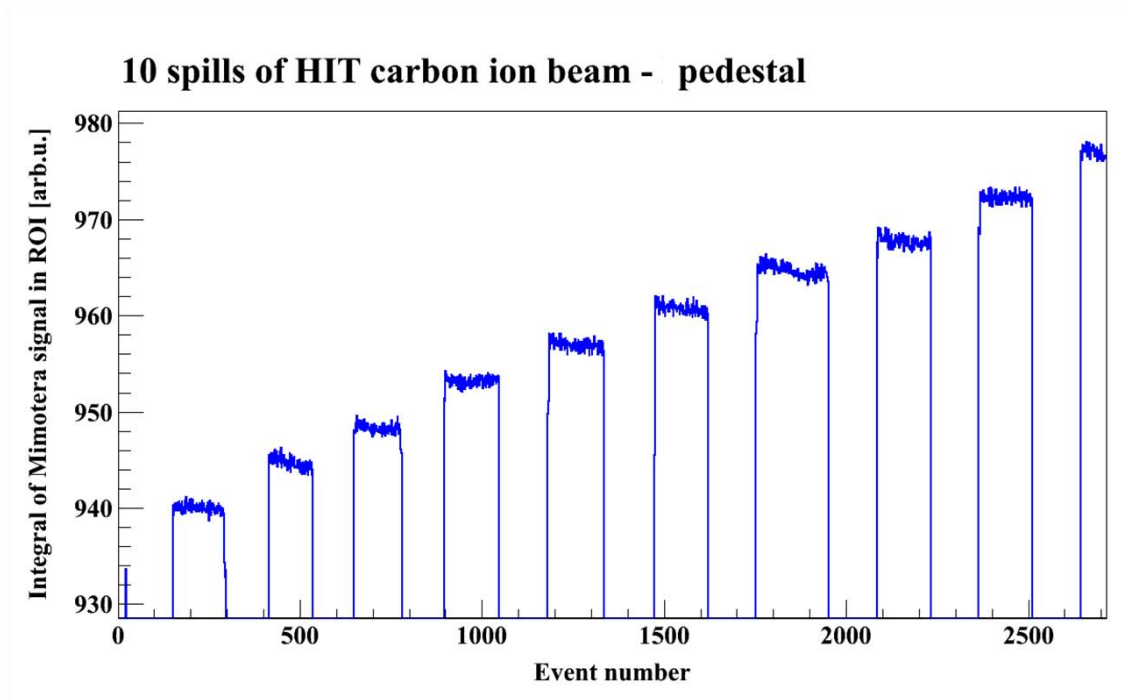


Figure 5.5: Time dependent pedestal at HIT in October. This is a zoom of Fig. 5.3, in order to visualize the decrease of the pedestal after every shot, the actual beam lies outside the range of the y-axis.

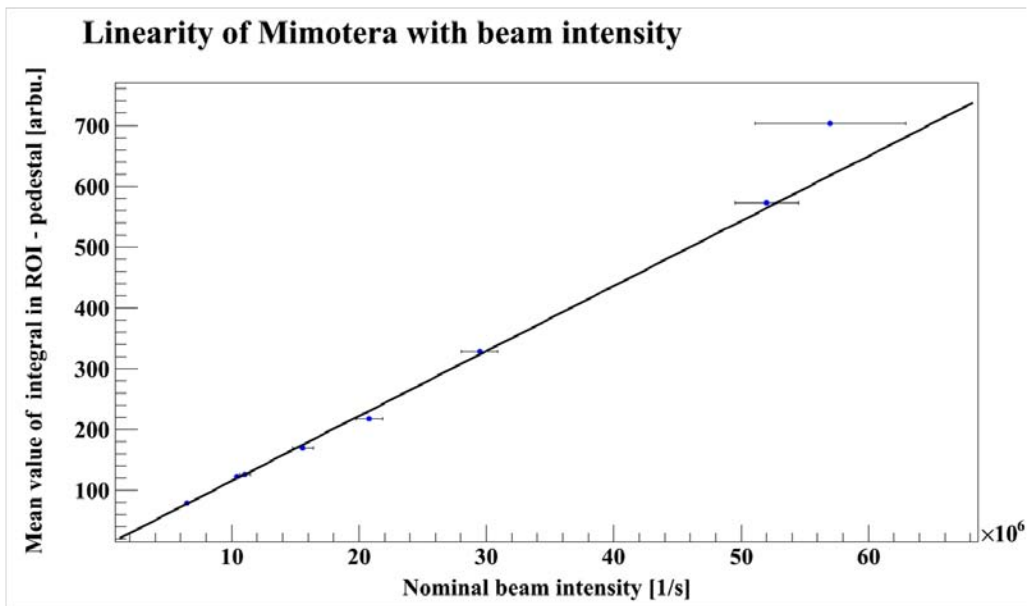


Figure 5.6: Linearity of the Mimotera signal for an intensity scan for carbon ions.

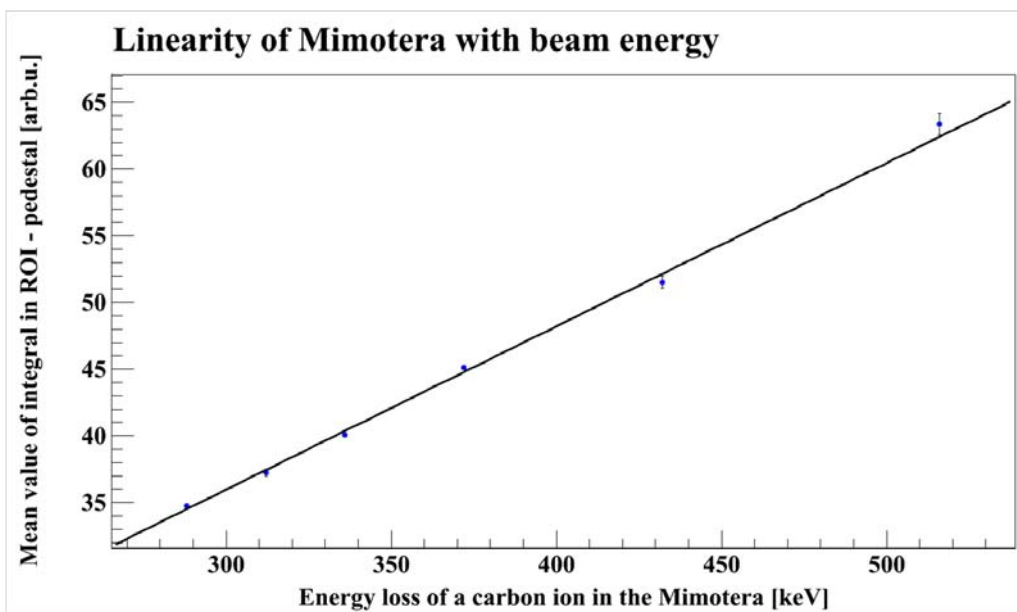


Figure 5.7: Mimotera signal for different beam energies.

### 5.3 Protons

The Mimotera has also been tested with a proton beam at HIT. The energy was 211.42 MeV with the smallest available focus size of 8.1 mm FWHM. A similar intensity correction as for carbon ions has to be done for the protons as well. It has been observed that the signal for protons is substantially lower than for carbon ions, although the proton intensities are about two orders of magnitude higher, see section 5.1. The reason is found to be the energy loss, that is different for protons and carbon ions.

Projectile		Target		Stopping Power:	
Charge [e]:	6	Silicon		2.443 z <sup>2</sup> MeV cm <sup>2</sup> /g	
Energy:	410 MeV/n	Z/A	I	Energy Deposit:	
		.498478	173.0	87.964 MeV cm <sup>2</sup> /g	
Mass [amu]:	12	Thickness: .0033 g/cm <sup>2</sup>		Total dE: 0.024 MeV/n	
Help		Total dE		File	
				Exit	

Figure 5.8: Energy loss of a 411 MeV/n carbon ion in 14  $\mu\text{m}$  of silicon.

Projectile		Target		Stopping Power:	
Charge [e]:	1	Silicon		3.516 z <sup>2</sup> MeV cm <sup>2</sup> /g	
Energy:	211 MeV/n	Z/A	I	Energy Deposit:	
		.498478	173.0	3.516 MeV cm <sup>2</sup> /g	
Mass [amu]:	1	Thickness: .0033 g/cm <sup>2</sup>		Total dE: 0.012 MeV/n	
Help		Total dE		File	
				Exit	

Figure 5.9: Energy loss of a 211 MeV/n proton in 14  $\mu\text{m}$  of silicon.

The density of silicon is  $2.33 \text{ g/cm}^3$  which results in an effective thickness of the sensitive volume of the Mimotera of  $2.33 \text{ g/cm}^3 \times 14 \times 10^{-4} \text{ cm} = 0.00326 \text{ g/cm}^2$ . The total energy loss of carbon ions and protons in the epi-layer of the sensor has been calculated with `bbt` [25] and is shown in Figures 5.8 and 5.9. Displayed is the total energy loss, electronic and nuclear, though the latter is negligible as it is three orders of magnitude smaller. In 14  $\mu\text{m}$  of silicon a carbon ion loses  $12 \times 0.024 \text{ MeV/n} = 288 \text{ keV}$ , that equals  $288 \text{ keV}/3.6 \text{ eV} = 8 \times 10^4$  electrons created in the epi-layer for an averaged band gap in silicon of 3.6 eV, see section 2.2.1. A proton loses 12 keV, corresponding to  $12 \text{ keV}/3.6 \text{ eV} = 3 \times 10^3$  electron-hole pairs. So the energy loss of a carbon ion in the Mimotera is 24 times bigger compared to a proton. The dynamic range of the Mimotera has been calculated in 3.4 to be

$5 \times 10^3$  to  $6 \times 10^6$  electrons per pixel per frame. Therefore, the energy deposition of a 211 MeV proton is not big enough to be detected as a signal.

Unfortunately, it was not possible to do measurements for lower proton energies at HIT, where the energy deposition would have been higher, because the minimal focus size of the beam increases rapidly with decreasing energy, resulting for example in a minimum focus of 32.4 mm FWHM for 50 MeV protons. As the Mimotera is only  $17 \times 17$  mm large, it appeared not useful to apply these conditions.



## 6 Open Questions and Summary

### 6.1 Radiation Damage

An effect that is not yet entirely investigated for the Mimotera is the influence of ion irradiation on the detector response. The variety of temporal and eventually permanent modifications occurring during the monitoring of protons, antiprotons and carbon ions will in the following be referred to as radiation damage. The main effect caused by the irradiation of a crystal lattice with nuclei is the displacement of atoms in the lattice, leading to interstitials, which are atoms in places in between two lattice points, and vacancies, which are empty lattice points. These have two consequences: They act as so called generation-recombination centers, which means they can capture and emit electrons and holes, leading to an increased leakage current in the space charge region. Moreover, they act as trapping centers for the signal charge carriers, causing a delay of the detection, and a decrease of the signal. See [24] for more details.

#### Ion beams at HIT

In Fig. 6.1, the analog output of the Mimotera immediately after two different days of irradiations with protons and carbon ions at HIT can be seen. The total irradiation time was about two hours for all runs, the beam intensity has been scanned to study the linearity of the detector response. For the first test on May 20, 2010 there is a clear increase of the background signal at the same position on the sensor where the carbon ion beam had been placed. This reaches up to the level that hit pixels are even saturated when using the unattenuated configuration of the Mimotera, as can be seen in the upper part of Fig. 6.1. Also, the position of the proton beam, which had been shifted with respect to the carbon beam is visible after the irradiation.

This impression can be quantified by analyzing the integral of the signal in a region of interest at the beam position, as explained in section 5.2. The result in Fig. 6.2 shows the absolute value of the pedestal, i.e. the signal height per pixel that decreases after every spill of carbon ions. This corresponds to an increase of the background, as the signal in the Mimotera is negative. The cause for this are probably generation-recombination centers in the silicon crystal, as mentioned above. The defects in the crystal lattice are electrically active and cause a capture and re-emittance of electrons that is visible in the analog output.

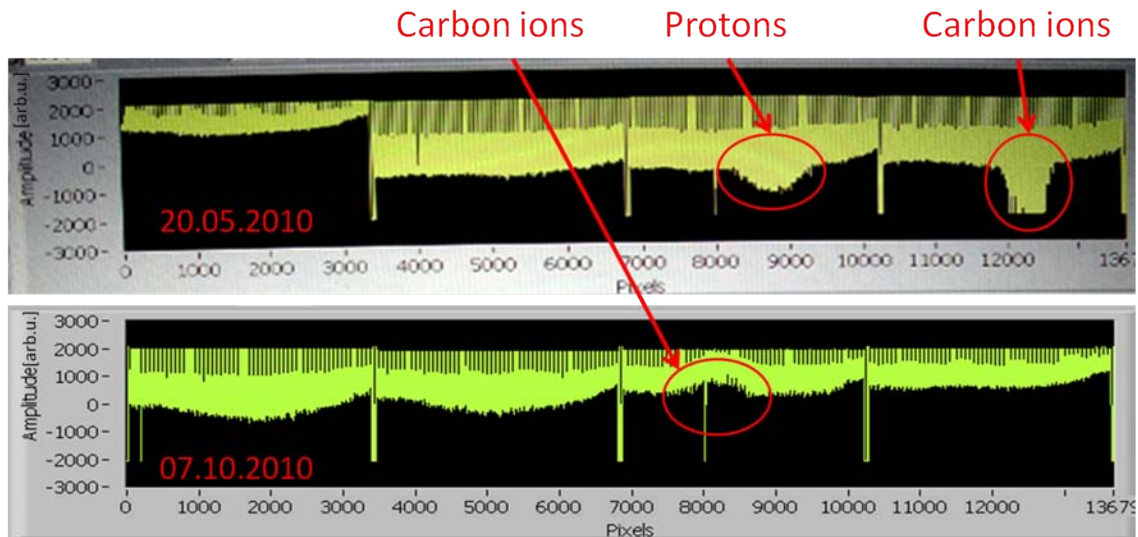


Figure 6.1: Background signal after two different irradiations of the Mimotera with protons and carbon ions.

The behavior illustrated in Fig. 6.1 has been found to decrease within a few hours after the irradiation, and it was not visible any longer in the analog output after two days. This is known as annealing, [24] caused by the fact that the defects are not stable, but mobile at room temperature. Therefore an interstitial and a vacancy can recombine, reducing the number of defects in the crystal lattice.

What is not yet understood is the fact that with a similar experimental set-up, a very different behavior has been observed for the run on October 7, 2010 that is illustrated in the lower part of Fig 6.1. The irradiation with a carbon ion beam now causes a dip in the background signal. This can be seen also in Fig. 5.5, in results of the data analysis from October, as the pedestal shows in this case the opposite behavior as compared to Fig. 6.2. The absolute value increases, resulting in a decrease of the background.

The only difference between the two measurements was that the PCB1 detector was used in May, and the PCB2 detector with the modified operational amplifier as explained in section 4 was used in October. Additional to the intensity scan that was the same for both runs, in October also an energy scan from 150 MeV/n to 400 MeV/n has been performed.

Moreover, although the change of the background signal is not visible any more in the analog output of the system within two days after the irradiation, it seems that it does not disappear completely. Irradiation of the same sensor with diffused room light some days later showed an effect like an apparent increase of sensitivity in the pixels where the ion beam had been. The signal did not rise evenly everywhere in the sensor, but a “spot” appeared, see Fig. 6.3.

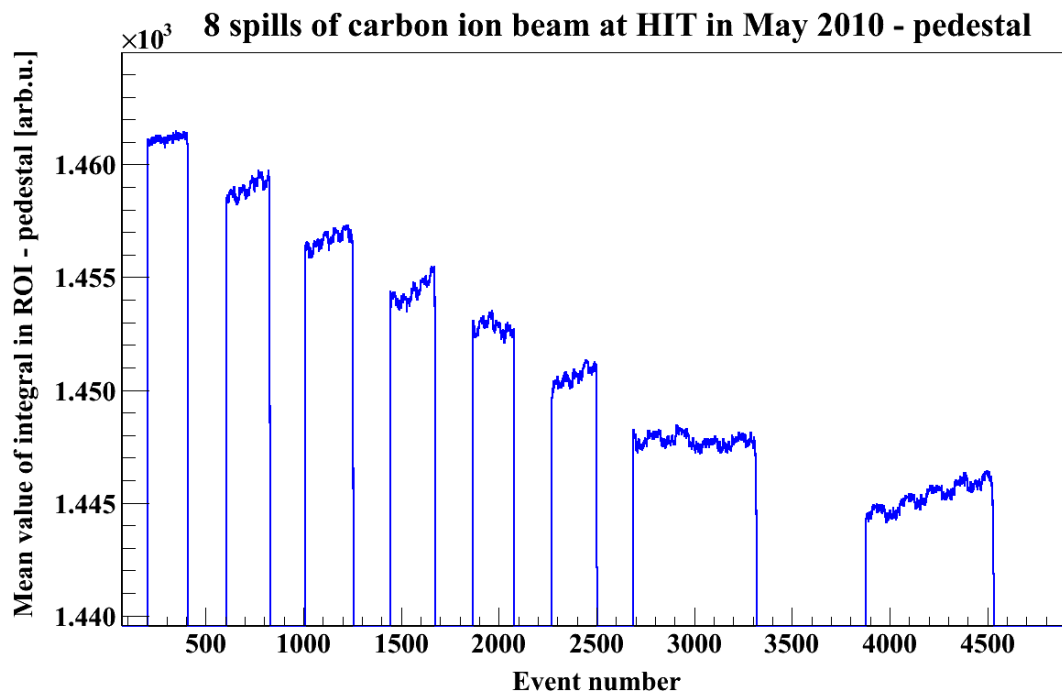


Figure 6.2: Time dependent pedestal at HIT in May. This is a zoom in order to visualize the background signal, the actual beam lies outside the range of the y-axis.

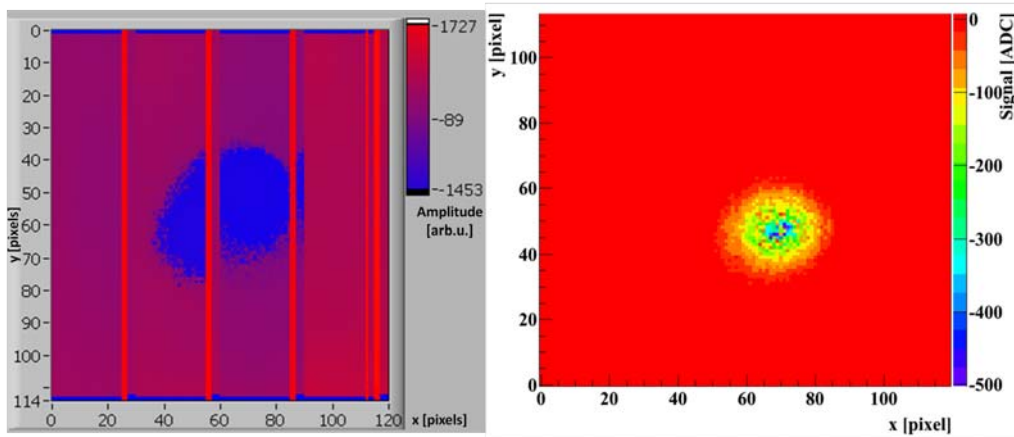


Figure 6.3: On the left, the signal in the Mimotera from diffuse room light falling on the sensor, after the increased background signal from the irradiation with carbon ions had already disappeared. On the right, a carbon beam spot from the corresponding run before is shown.

## Antiproton beam at ACE

The number of particles delivered to the sensor during one week of beam time at ACE is by no means comparable to one day of beam time at HIT, because at ACE one spill lasts 500 ns and comes only every 90 s. No change in the background signal is found. Nevertheless, another interesting observation can be made with these different beam characteristics. Remember the binary structure of a data file recorded by the Mimotera, as explained in Fig. 3.6. In between two events in one file lay 90 s, because one event is recorded for each trigger pulse of the AD. Take also into account, that the data is analyzed in a differential way, providing for example differences of frames 3-1, 5-3, etc. for matrix B, see Fig. 3.4. When this difference is taken for every two subsequent frames in a data file, and if 38 frames are recorded for each event, then the difference of frames 39 and 37 in the file monitors the change of the signal within a 90 s time frame. In other words, the last (empty) frame of event 1 is subtracted from the first (empty) frame of event 2. The result that is being observed for this difference is shown in Fig. 6.4.

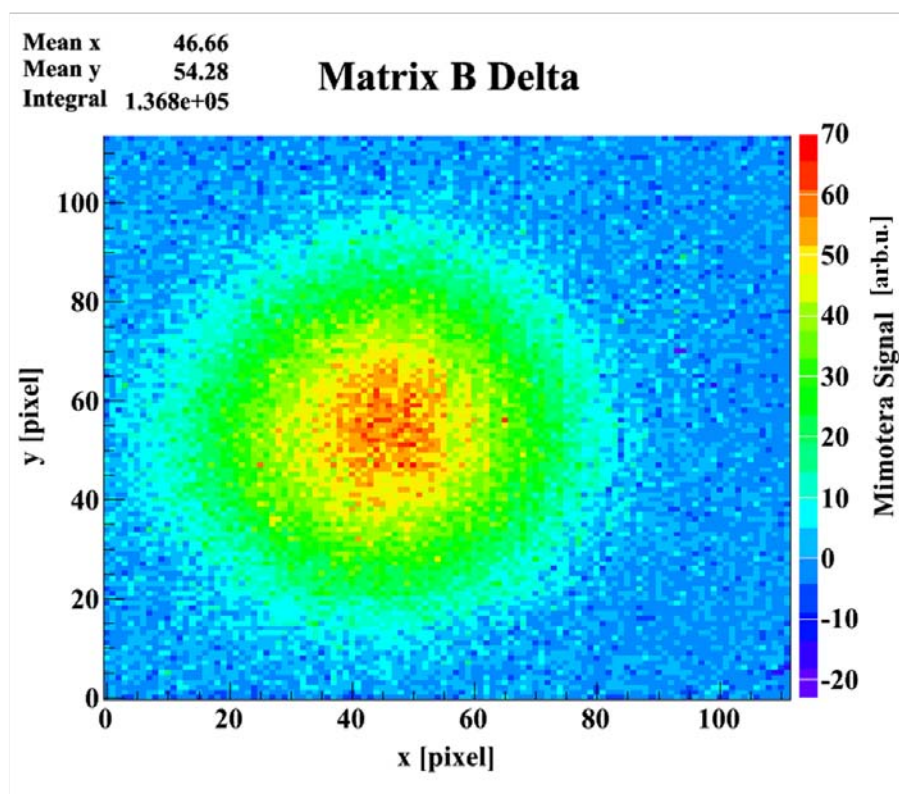


Figure 6.4: Difference of the Mimotera signal during 90 s after the beam spill, for the matrix in which the beam was recorded.

The specific readout matrix in which the beam spill was recorded for event 1, shows a spot sized signal when evaluating the difference between the last frame of event one and the first frame of event two 90 s later. The same difference taken for the matrix in which no beam was recorded shows only noise. As the diodes of both matrices have been equally irradiated by the beam, this can not be an effect of crystal damage in the silicon. It is likely to be an incomplete readout of the signal charges in the electronics. It can be concluded that  $(37 - 7)/2 = 15$  readout frames of one sub-matrix are not sufficient to collect every charge carrier generated. The decrease within 90 s of the exponentially decaying signal height in the matrix is what is being observed here.

Finally, one should mention that even though the observed modifications of the detector response as a function of irradiation time and characteristics should be ultimately understood, they do not have any substantial influence on the operation of the Mimotera as beam profile and intensity monitor for all practical purposes. Any irradiation effect found in the course of this thesis was affecting the signal significantly after optimization of the electronic readout.

## 6.2 Summary and Outlook

The Mimotera, a monolithic active pixel sensor, has been successfully installed and tested as a beam monitor for the Antiproton Cell Experiment at CERN. The system provides a major improvement for the experiment, not only in terms of a more reliable data analysis, but also for a faster initial set-up of the experiment due to online, shot-to-shot monitoring of the beam. After optimization, it was proven to operate without saturation. Moreover, it is possible to see the beam on a second Mimotera installed behind the first one at the end of the experimental table, allowing a more efficient alignment of the table in the future. For a reliable and stable operation of the Mimotera at ACE, the problems of the electronics have to be solved that caused the discontinuities in the October 2010 run. This is currently still under development.

The Mimotera furthermore shows promising results in monitoring continuous clinical ion beams as in use at the Heidelberg Ion-Beam Therapy Center. For an application as a quality assurance tool it is preferable to increase the active area by mounting four sensors on the same chip. If one would like to use the sensor not only for quality assurance, but for monitoring the beam during patient treatment, it would be necessary to remove the PCB background directly behind the sensor and maybe even thin down the silicon support further, in order to reduce beam straggling. Moreover, the radiation hardness of the system has to be better understood. Detailed and systematic tests of the behavior of the background signal are needed to understand the effects described in the previous section.



# Appendix



# A Mimotera Manual for ACE

## Handle with care!

- **The sensor must never be touched with anything!** There are very thin wires connecting the PCB background to the sensor, which can be easily unbonded. If the chip has to be unmounted from the holder for some reason, touch only the PCB and only on the edges. Be extremely careful with the screwdriver, side-slipping may cause irreparable damage.
- When changing cell samples in the water tank, please, make sure that no liquid gets in contact with the sensor, the data acquisition board or the laptop.
- The whole system is sensitive to motion. Shocks or moving the system while running might cause a crash of the data acquisition. Do not stress the green cable, it is very sensitive and has to hang loose all the time.

If there is a crash of the program, do the following:

1. Close LabView
2. Close CyConsole
3. Turn off the power supply and wait a few seconds.
4. Turn it back on and continue with “Setting up the system” below.

## A.1 Setting up the system

### Installation of the DAQ Software

1. Install LVRuntimeEng.exe
2. Install Cypress USB console
3. Copy the file CyUSB.inf (in the Cypress installer folder) in C:/programs/cypress/USBDevStudio/Driver
4. Connect the system to the PC. (See also next paragraph) Turn on the power supply. The first time, Windows asks for drivers. Select “No, not this time” in the installation wizard. Then chose the path of the cypress’ drivers folder as above.

## Setting up the System

1. Make sure that the power supply has the correct voltage and current limits set: Turn it on without the DAQ board connected to it. Check that the voltage applied is 7V. Short circuit the poles with a cable and make sure that the current limit is 1.5 A maximum. Fix the knobs with tape. Re-remove the cable and turn the power supply off.
2. Connect all cables between sensor, DAQ board, power supply and PC. On the cable between DAQ board and power supply, black is ground, red is positive. Connect the trigger cable to the DAQ board. The two correct pins are marked in Fig. A.1 and the cable has to be connected in a way that the white text on the connector is outside the two rows of pins, not in between. Do not connect it to the AD-trigger yet, because then the system will react to any changes you apply in the LabView front panel only every 90 s.
3. Turn on the power supply.
4. Check the values of the voltages VREF1 and VREF2 on the DAQ board with a multimeter. They should be maximal, that is 4.45 V or 5 V, depending on the version of the DAQ board. They can be set using a small screwdriver to adjust the potentiometers on the DAQ board, labeled VREF1 and VREF2.
5. Open the Cyconsole. Select Options → EZ-USB Interface → Download. Select the file `Synchro.hex`. Find `AltSetting` on the interface, type in 1 and press enter.
6. Run the executable of the LabView data acquisition software from the desktop. (Current version GUI 6.91.exe)

## Finding the Correct Settings

The VMR voltage also has to be adjusted with a screwdriver directly on the DAQ board. Its value depends on the attenuation factor and on several other factors and therefore has to be checked every time. To find the correct value, look at the x-y spectrum tab in the LabView front panel (see Fig: A.5) while turning the screw for the VMR on the board. Observe the changes this causes in the spectrum.

The end of the dynamic range of the sensor is marked by the marker pixels and the spectrum of the pixel signal lies in the middle. The VMR voltage should be selected in a way that no part of the spectrum is “squeezed” to the right or left edge and that the dynamic range is as large as possible. Note that the signal in the Mimotera is negative.

Also look at the x-y-amplitudes tab, (see Fig. A.4) make sure that the amplitudes are not “squeezed” at the top and that the range to the bottom is as large as possible. The baselines of all four quarters should be equal.

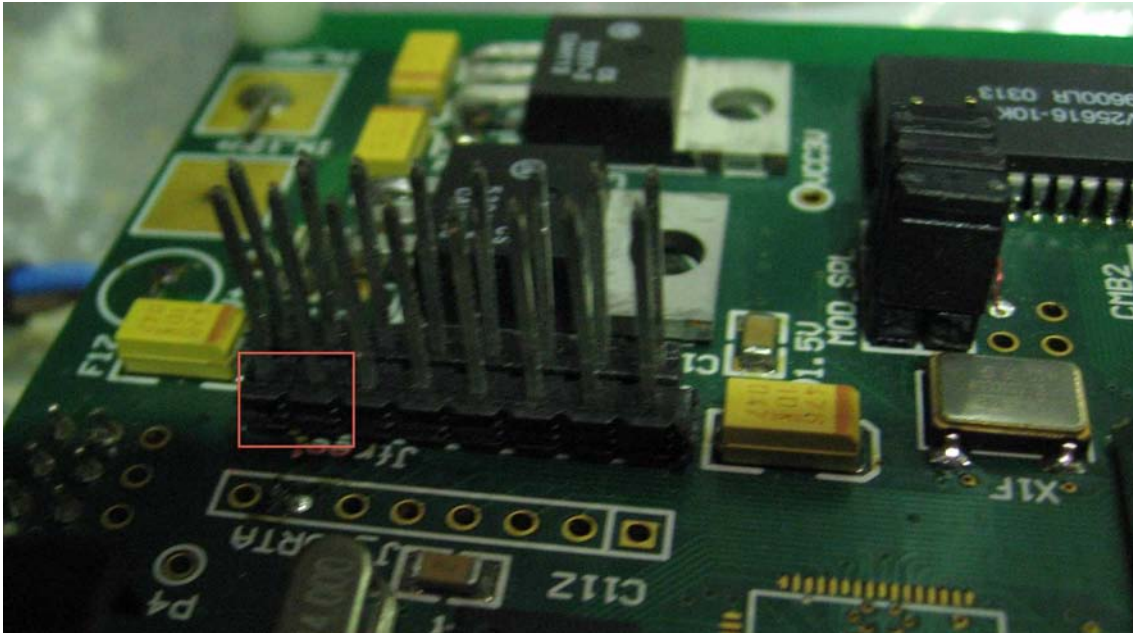


Figure A.1: The two pins that have to be used for triggering the DAQ board.

## A.2 Taking Data

1. Enter the correct settings of all parameters on the LabView front panel that can be seen in Fig. A.2.
  - Check Mkoff and Mkoff2 in order to avoid influences of the digital outputs on the analog signal.
  - Uncheck SO.
  - Check PCB Hybrid if a PCB system is in use.
  - Uncheck AT, unless you would like to attenuate the signal height by a factor of about five.
  - Select Post-reset pulse = 6 in order to have the marker pixels in the right positions.
  - Select Reset pulse width = 3
  - Select ADC clock delay = 1
  - Select the desired number of frames to save after each trigger. (“after trig. fr. amount”) and before each trigger. (“after trig. fr. amount”). The sum of both can be maximum 38. If you save for example 6 frames before each trigger, it means that the beam spill is always contained in frame number 7.

- Press the button const/trigger in a way that it is dark green, not light green.
- Select  $\text{ADC-CLK} = 2.5 \text{ MHz}$

Afterwards, click “Send Parameters”, preferably two or three times to be sure the input was accepted.

2. Now connect the cable to the AD trigger. Everything else can then be done remotely from outside the zone.
3. Enter how many events you would like to save (“no. of events to store”, Fig. A.2). This is the number of events that will be saved to one data file. At ACE, each event corresponds to one trigger pulse of the AD, one event is saved every 90s. To obtain the number of frames that are stored, multiply the number of events by [(after trig. fr. amount) + (before trig. fr. amount)]. Note that one event consisting of 38 frames needs roughly 2 MB and that a data file must not exceed 2 GB.
4. Enter the full path of the file including the extension `.dat` at the interface, see Fig. A.2. If you do not change the filename in between two runs, the first file will not be overwritten but the data is attached to the first file.
5. Click “save to file”. As soon as the next trigger pulse arrives, the green light will light up and “no of events to store” will start counting down from the value you entered to zero. If you wish to stop the data taking earlier, press “stop saving”. In this case the number will immediately jump to 1 and the file will be finished after the next trigger pulse that arrives.

To see the beam online on the front panel, make sure that the following adjustments are correct:

- On the X-Y-Subtract tab on the right in Fig. A.2, the difference has to be taken between the frame that contains the beam spill and the previous one. If 6 frames are saved before each trigger, this has to be relative frame number 7 minus 6.
- The beam can be in matrix A or in matrix B. If you do not see anything, try changing “matrix to subtract” from  $A(x)-A(y)$  to  $B(x)-B(y)$  in the same tab.

Now you should be able to see the beam in the X-Y-Subtract tab as in Fig. A.6.

Looking at the tab Beam on-line imaging in Fig A.7, in order to see the beam, make sure that:

- No. to sum up for display is 1. Otherwise several events are summed up until you can see the beam.
- Analog to the X-Y-Subtract, change between matrix A and B in case the beam was recorded in the other matrix.

When an adjustment of the beam is necessary, consider the following: The picture of the beam that is visible on the interface is what you see when you stand behind

the Mimotera and look into the beam. This means that up/down are correct, but left/right are reversed from the beam's eye point of view (which normally is also the operator's view).

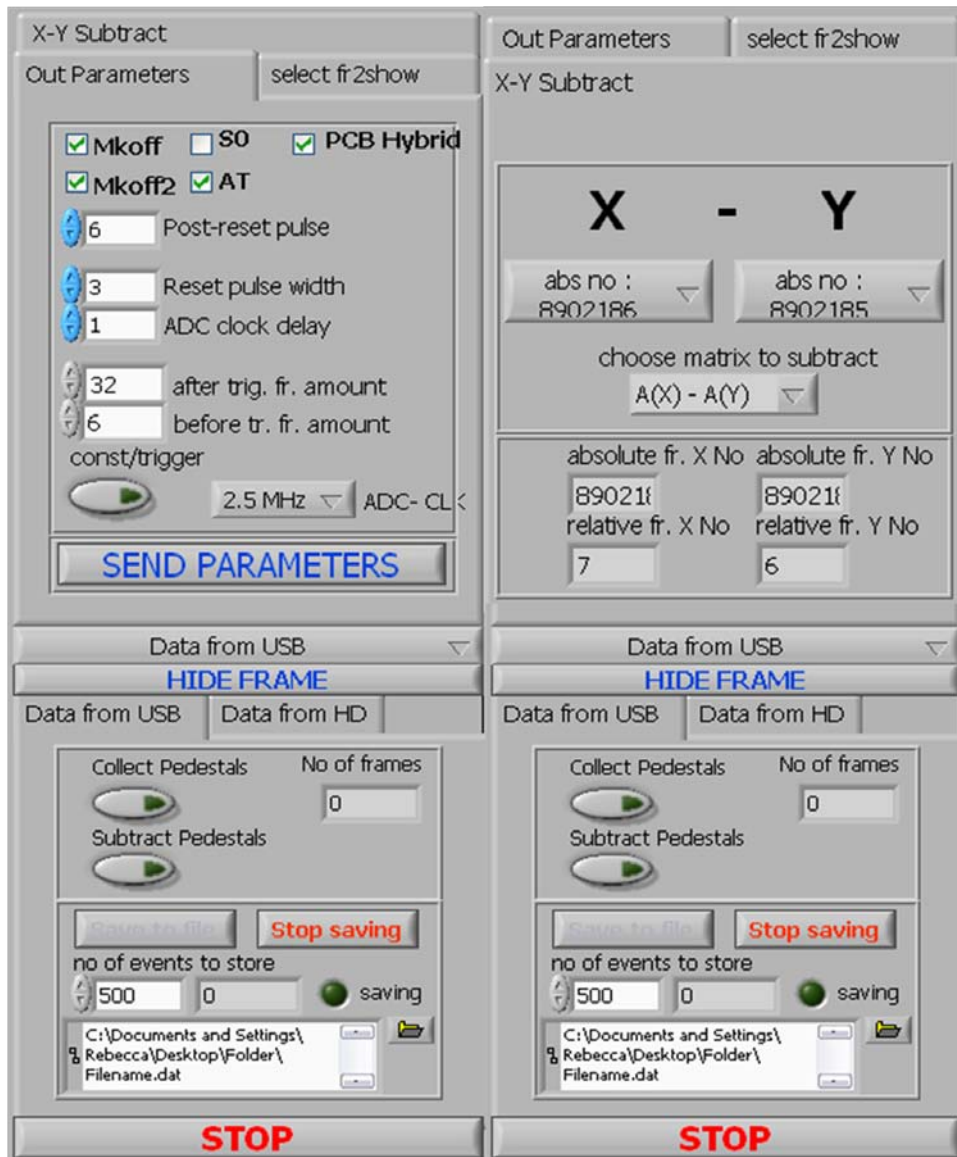


Figure A.2: Choosing the right Parameters for the measurements at ACE.

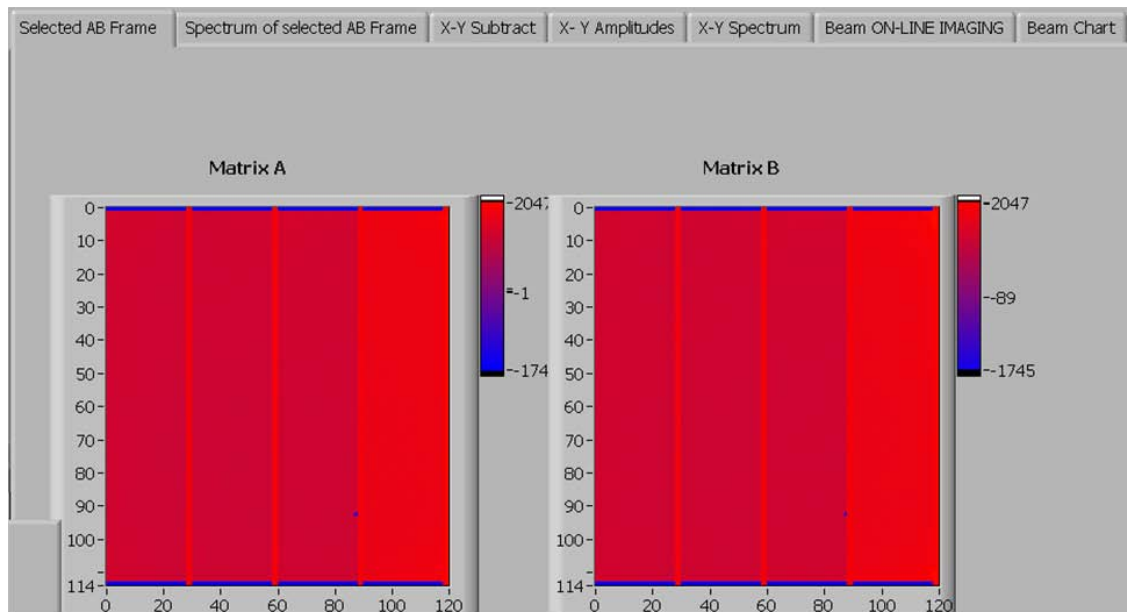


Figure A.3: Selected AB frame in LabView.

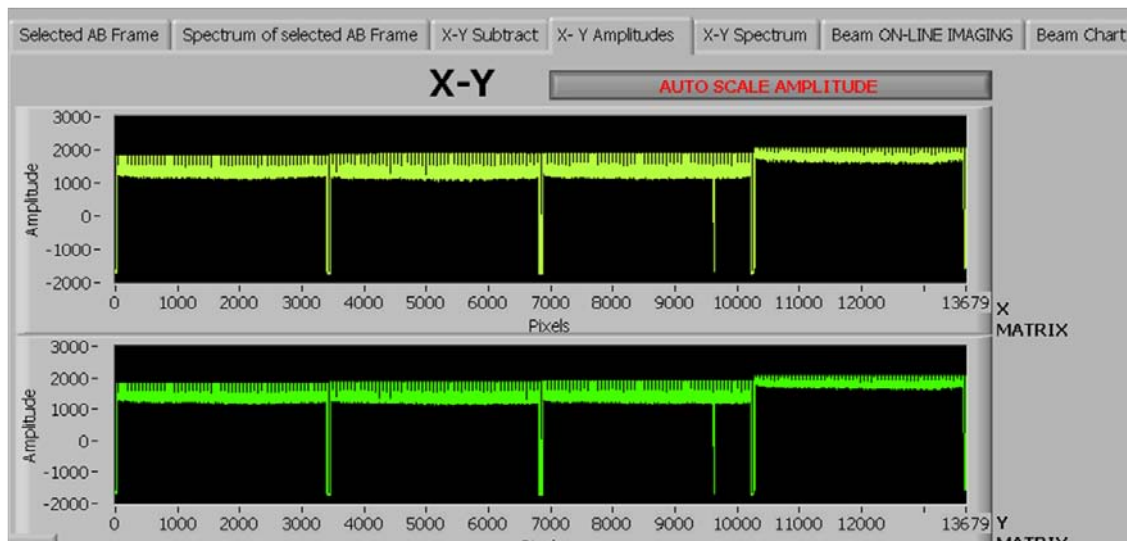


Figure A.4: X-Y-Amplitudes in LabView.

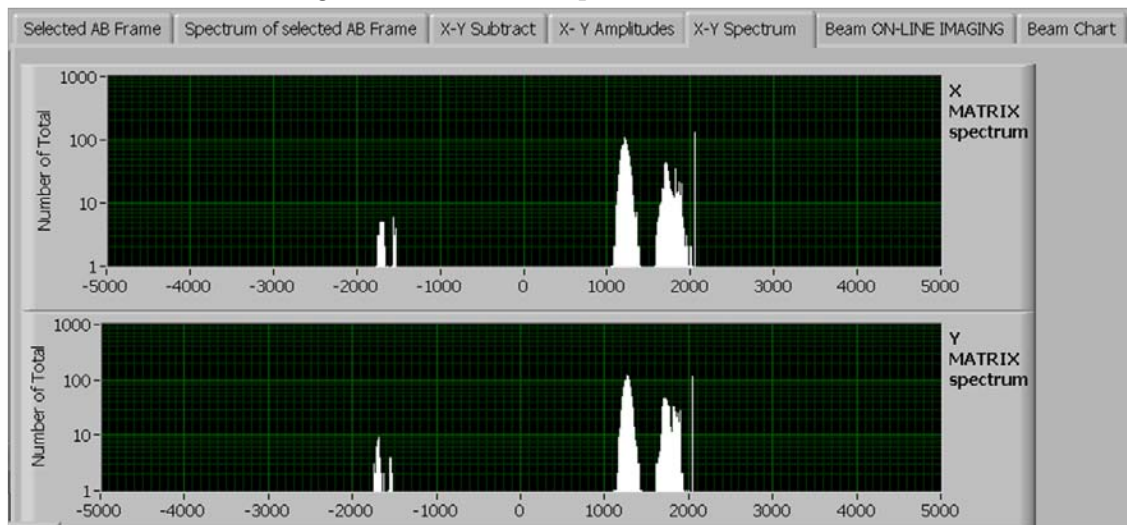


Figure A.5: X-Y-Spectrum in LabView.

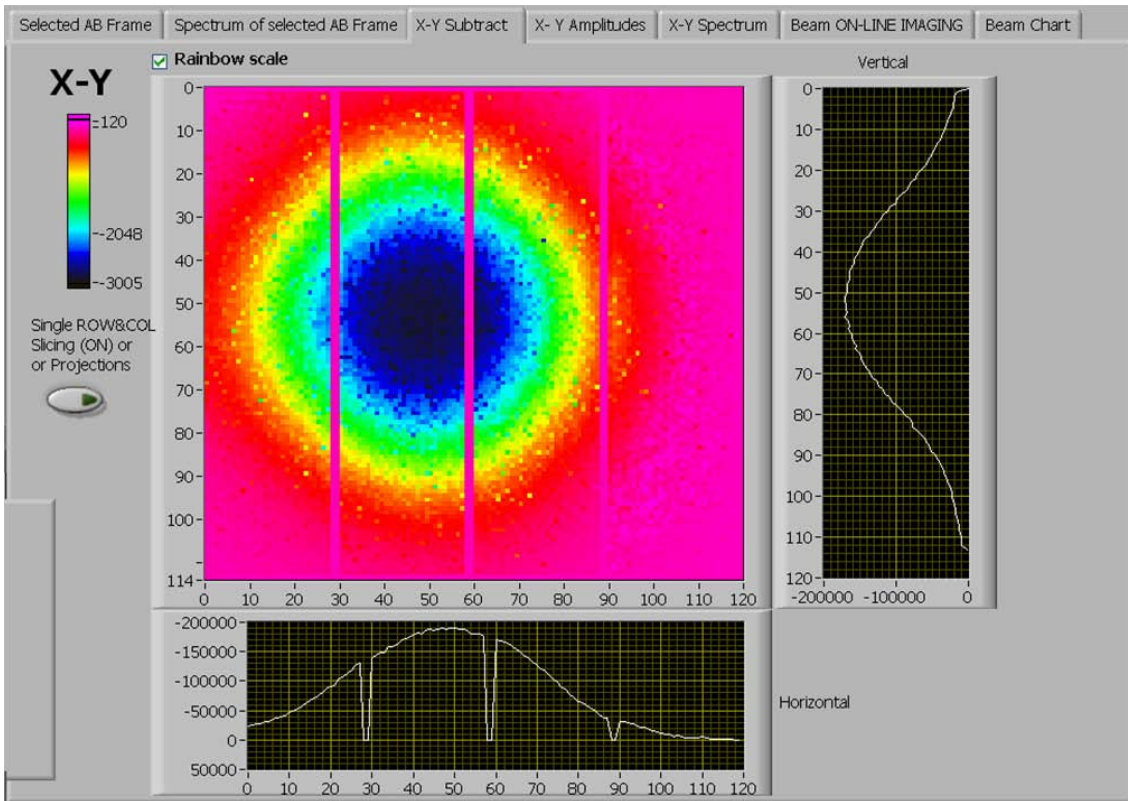


Figure A.6: X-Y-Subtract in LabView.

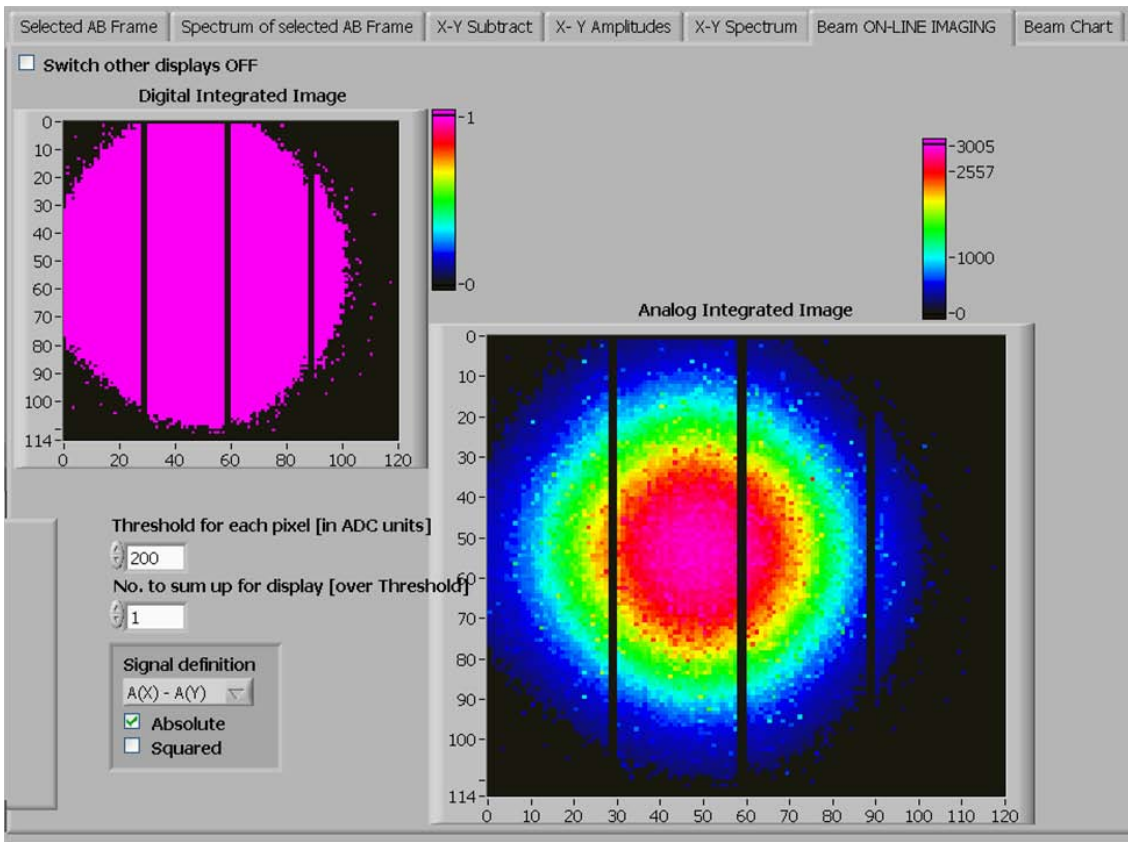


Figure A.7: Beam on-line image in LabView.



## B Bibliography

- [1] Particle Data Group: Review of Particle Physics. *University of California, 2010.*
- [2] G. Kraft: Tumor therapy with heavy charged particles. *Prog. Part. Nucl. Phys.* 45, 2000.
- [3] <http://ptcog.web.psi.ch/>
- [4] M. Henley, A. Garcia: Subatomic Physics. *World Scientific Publishing Co. Pre. Ltd., Singapore. 3. edition, 2007.*
- [5] W. H. Bragg and R. Kleemann: On the Ionization Curves of Radium. *Phil. Mag.* 8, 1963.
- [6] S. Sellner: Real-Time Imaging of the Annihilation Vertex Distributions for Antiprotons Stopping in Biological Targets. *Diploma thesis, 2010.*
- [7] T. E. Kalogeropoulos, R. Muratore: Antiprotons for Imaging and Therapy. *Nucl. Inst. Meth. B40/41, 1989.*
- [8] M. Holzscheiter et al.: The Biological Effectiveness of Antiproton Irradiation. *Radiotherapy & Oncology* 81, 2006.
- [9] S. Maury: The Antiproton Decelerator: AD. *Hyperfine Interact.* 109, 1997.
- [10] B. G. Wouters, G. K. Lam, U. Oelfke, K. Gardey, R. E. Durand, L. D. Skarsgard: Measurements of relative biological effectiveness of the 70 MeV proton beam at TRIUMF using Chinese hamster V79 cells and the high-precision cell sorter assay. *Radiat. Res.* 146, 1996.
- [11] <http://www.tera.it/ise.cgi>
- [12] [http://www.bergoz.com/index.php?option=com\\_content&view=article&id=14&Itemid=17](http://www.bergoz.com/index.php?option=com_content&view=article&id=14&Itemid=17)
- [13] M. Martisikova, B. Ackermann, S. Klemm, O. Jäkel: Use of Gafchromic EBT films in heavy ion therapy. *Nucl. Inst. Methods Phys. Res. A* 591, 2008.
- [14] S. M. Sze: Physics of semiconductor devices. *Wiley, New York. 3. edition, 2007.*
- [15] S. Hunklinger: Festkörperphysik. *Oldenbourg Wissenschaftsverlag, München. 1. edition, 2007.*

- 
- [16] P.Riedler: Lecture on Silicon Pixel detectors. *Geneva, 2006/2007*.
- [17] [http://www-m2.ma.tum.de/homepages/gilg/notesd/Vorl\\_S\\_K1.pdf](http://www-m2.ma.tum.de/homepages/gilg/notesd/Vorl_S_K1.pdf)
- [18] <http://en.wikipedia.org/wiki/Scintillator>
- [19] L.Bandano: Developpement d'un moniteur de faisceau innovant pour la mesure en temps reel des faisceaux utilises en hadron therapie. *PhD thesis, 2005*.
- [20] <http://root.cern.ch/drupal/>
- [21] V. Radeka: Low-noise techniques in detectors. *Ann. Rev. Nucl. Part. Sci. 38, 1988*.
- [22] C. Brusasco, B. Voss, D. Schardt, M. Krämer, G. Kraft: A dosimetry system for fast measurement of 3D depth-dose profiles in charged-particle tumor therapy with scanning techniques. *Nucl. Inst. Methods Phys. Res. B 168, 2000*.
- [23] P. Riedler, J. Rochet, A. Rudge, M. Doser, R. Landua: Performance of ultra-thin silicon detectors in a 5 MeV antiproton beam. *Nucl. Inst. Methods Phys. Res. A 478, 2002*.
- [24] G. Lutz: Semiconductor Radiation Detectors. *Springer-Verlag, Berlin Heidelberg, 2007*
- [25] <http://www.sgeier.net/tools/bbt.html>

# Acknowledgments

At this point I would like to thank everybody who supported my work during the last year, and who contributed to this thesis in any way:

Michael Holzscheiter, for always giving good answers and posing the right questions, and for believing in me in moments I didn't.

Joachim Ullrich, for having helpful suggestions and questions, and for improving the result of this thesis.

Oliver Jäkel, for always supporting my work and making the measurements at the Heidelberg Ion-Beam Therapy Center possible.

Massimo Caccia, for enabling this work in the first place, by providing the detector along with a lot of first-hand advice and many emails; Loretta Negrini, for being of great help in measuring and analyzing data; and everybody else from this group at the Università dell' Insubria in Como, Italy.

The members of the QUASAR group at the Max-Planck-Institute for Nuclear Physics, Heidelberg, Germany; particularly Carsten Welsch, for his support and ideas.

The members of the E040-9 group at the German Cancer Research Center, Heidelberg, Germany, for good collaboration.

Stefan Sellner, for processing the simulations and for arbitrating between me and my computer.

Kirsten Vincke, Jana Schnieders, and Dennis Kütemeier, for finding hopefully every mistake I made.

Someone special, for never stopping to believe in me.



Erklärung:

Ich versichere, dass ich diese Arbeit selbstständig verfasst habe und keine anderen als die angegebenen Quellen und Hilfsmittel benutzt habe.

Heidelberg, den 1. Dezember 2010

.....

